Petrology and Volatile Content of Magmas Erupted from Tolbachik Volcano, Kamchatka, 2012-13

Pavel Plechov[1], Jon Blundy[2], Nikolay Nekrylov[1], Elena Melekhova[2], Vasily Shcherbakov[1], Margarita S. Tikhonova[1]

[1]Department of Geology, Lomonosov Moscow State University, 1 Leninskie Gory, 119992 Moscow, Russia. E-mail: pplechov@gmail.com

[2]School of Earth Sciences, University of Bristol, Wills Memorial Building, Bristol BS8 1RJ, UK. E-mail: lena.melekhova@bristol.ac.uk

Abstract

We report petrography, and bulk rock, mineral and glass analyses of eruptive products of the 2012-13 eruption of Tolbachik volcano, Central Kamchatka Depression, Russia. Magmas are shoshonitic in composition, with phenocrysts of olivine and plagioclase; clinopyroxene phenocrysts are scarce. Samples collected as bombs from the active vent, from liquid lava at the active lava front, and as naturally solidified "toothpaste" lava allow us to quantify changes in porosity and crystallinity that took place during 5.25 km of lava flow and during solidification. Olivine-hosted melt inclusions from rapidly-cooled, mm-size tephra have near-constant H_2O contents (1.19±0.1 wt%) over a wide range of CO_2 contents (<900 ppm), consistent with degassing. The groundmass glasses from tephras lie at the shallow end of this degassing trend with 0.3 wt% H_2O and 50 ppm CO_2. The presence of small saturation, rather than shrinkage, bubbles testifies to volatile saturation at the time of entrapment. Calculated saturation pressures are 0.3 to 1.7 kbar, in agreement with the depths of earthquake swarms during November 2012 (0.6 to 7.5 km below the volcano). Melt inclusions from slowly-cooled and hot-collected lavas have H_2O contents that are lower by an order of magnitude than tephras, despite comparable CO_2 contents. We ascribe this to diffusive H_2O loss through olivine host crystals during cooling. The absence of shrinkage bubbles in the inclusions accounts for the lack of reduction in dissolved CO_2 (and S and Cl). Melt inclusions from tephras experienced <3wt% post-entrapment crystallisation. Melt inclusion entrapment temperatures are around 1080 °C. Compared to magmas erupted elsewhere in the Kluchevskoy Group, the 2012-13 Tolbachik magmas appear to derive from an unusually H_2O-poor and K_2O-rich basaltic parent.

Highlights

- Magma erupted from the 2012-13 eruption of Tolbachik is basaltic trachyandesite
- Magmas are K_2O-rich and H_2O-poor compared to others from the Kluchevskoy Group
- Changes in magma texture and chemistry during a 5-km lava flow have been quantified

Keywords: Tolbachik fissure eruption, basaltic volcanism, shoshonitic magmas, melt inclusions, volatiles, degasing.

1. Introduction

Volcanic arcs above subduction zones rarely erupt primitive arc magmas whose compositions are consistent with derivation directly from the mantle wedge without subsequent chemical modification. Modern examples of primitive arc magmas are particularly rare, restricting our ability to see through the crustal processing of magmas to mantle-melting processes in the wedge itself. The 1975-76 Great Fissure Eruption of Tolbachik, Kamchatka, was one such example, with Mg# of 0.68 and MgO content over 14 wt% (Fedotov, 1984). This eruption offered petrologists a glimpse into the chemistry of the sub-Kamchatkan mantle wedge at a moment in time, with implications for its thermal and physical state. At the onset of the 2012-13 Tolbachik eruption there was interest in establishing the nature of the newly erupted magma, its pre-eruptive storage conditions and its possible genetic relationship to the 1975-76 magmas.

2. Geological setting

Tolbachik is situated within the Central Kamchatka Depression (Figure 1a, inset), forming part of the Kluchevskoy Group of volcanoes, the most active in the Kamchatkan arc. Tolbachik has been dormant since the end of the Great Fissure Eruption eruption, although fumarolic activity continued locally throughout this time. The Tolbachik 2012-13 eruption (named the "50th anniversary eruption" in honour of the Institute Volcanology and Seismology, Far Eastern Branch of the Russian Academy of Sciences) started on Nov 27, 2012 and finished on Aug 21, 2013. The first description of lava flow morphology, extrusion rates and volumes, and other volcanological features have already been published (Samoylenko et al., 2012; Edwards et al., 2013; Dvigalo et al, 2014, Volynets et al., 2013) and here we provide only a summary.

Over the first four days of the 2012-13 eruption lava erupted from the Menyailov group of vents (MGV, main cone located at N 55°47′9″, E 160°19′39″, 1900 m asl). After December 1, 2012,

and until its conclusion, the eruption continued from the Naboko group of vents (NGV, N 55°46′6″, E 160°18′59″, 1650 m asl). We visited the NGV during August 2013, shortly before the eruption ended, and the associated lava fields (Figure 1a): the large Leningradskoe lava field formed during late 2012- early 2013; the Toludskoe lava field, which was the last active lava field from NGV and source of all samples studied here. The earlier Vodopadnoe lava field, associated exclusively with MGV was not visited. Locations of the three lava fields and the samples recovered are shown in Figure 1a and listed in Table 1. Note that most samples were taken in duplicate, with a Moscow State University sample number (PK-13/*n* and NK-13/*n*) and a University of Bristol number (KAM-*n*). Field photographs of the eruption, including those from sampled localities, are given in Figures 1b-d. There was an overall change from explosively erupted material (bombs) from one of two small, ephemeral lava lakes at the vent (Figure 1b), through subterranean lava flow (skylights, lava tubes; Figure 1c) to effusive lava flows (a'a and pahoehoe flows, "toothpaste" lavas, and lobes; Figure 1 d,e) to the south-southeast. The western branch of the Toludskoe lava field (Figure 1a) was completely solidified at the time of our visit.

3. Analytical techniques

3.1. Sample preparation

Olivine grains with naturally quenched primary melt inclusions were selected from four samples: air-collected, tephra from NGV (NK-13/2, NK-13/3), very fresh solidified lava (PK-13/6) from the Toludskoe lava field, and liquid-collected lava (PK-13/7) from the active lava front. Air-collected tephra (ash) has particle sizes from 0.2 to several millimeters. Ash samples were sieved to 0.5-1 mm without crushing, whereas lava samples were gently crushed and sieved to 0.25-0.5 mm. Then olivine grains were picked out manually. Almost all olivine grains in the size fraction contain glassy melt inclusions (MI). We selected only olivines containing large (>35 μm) glassy MI with small or no shrinkage bubbles. After picking, 30 MI-bearing olivine grains from the tephra were leached in HF for 10 min to dissolve the dark glassy rim around each grain to make it transparent. We then conducted eight thermometric experiments with a Linkam-TS1500 stage to determine optimum melt inclusion quenching temperatures. During thermometric experiments MI devitrify during heating in the temperature range 540-610 °C, then melt in the 1020-1120 °C range. The last crystals dissolve at 1130-1200 C in different experiments.

The Linkam-TS1500 stage lacks the capability for rapid quenching. For this reason selected MI were reheated and quenched at Moscow State University in a specially designed furnace mounted inside a firebrick. The heater consists of an Alundum® cylinder 20 mm in diameter and

50 mm long with 40 winds of 0.5 mm platinum wire. A fused quartz sample stage is placed in the middle of the furnace. The work-space (thermo-camera) has a diameter of 18 mm, with a Pt-$PtRh_{10}$ thermocouple inserted 0.5 mm below the stage. Acid-leached olivine grains are placed onto a rectangular platinum sample cell, and each grain covered with a graphite cap. The platinum cell is inserted into the furnace, which is heated to a desired temperature in advance, with temperature control by a MasTech HY-3020E DC power supply. When a sample is placed into the cell, temperature usually drops by 5–10 K and recovers in less than 2 min. For our quenching experiments the furnace was set at the highest temperature obtained from thermometric experiments or at 20 °C above calculated olivine-melt equilibrium temperature for better kinetics. Samples are quenched by extracting the platinum cell from the furnace. The sample is estimated to cool by 400–600 °C within the first second. The thermocouples are calibrated to the melting points of pure gold, bismuth, copper, silver, and cadmium. Typical errors on experimental temperatures are <0.5%. Horizontal temperature gradient inside the furnace is <3 °C for the full working diameter at the melting point of gold. Duration of each experiment did not exceed 8 min, to minimize diffusion of volatiles away from the inclusions.

3.2. Secondary ion mass spectrometry (SIMS)

H_2O and CO_2 contents of glassy melt inclusions, mounted in low-volatility resin, were analyzed by secondary ion mass spectrometry (SIMS) using a Cameca IMS-4f instrument at the NERC ion microprobe facility, University of Edinburgh, UK. Analyses were performed with a nominal 10 kV primary beam of O^- ions and a beam current of 5 nA giving a ~ 20 µm diameter spot at the sample surface. H_2O was measured as $^1H^+$ secondary ions at a nominal mass resolving power (M/ΔM) of 300 and a 25 µm image field. For CO_2, measured as $^{12}C^+$, a higher mass resolution of 800-1000 was applied, to differentiate between $^{24}Mg^{2+}$ and $^{12}C^+$, and a 20 µm image field used. Positive secondary ions were extracted at 4.5 kV with an offset of 50 V (for C) and 75 V (for H) to reduce transmission of molecular ions. Pumping to a vacuum of $\leq 10^{-9}$ Torr minimized the background to ~6 counts per second for ^{12}C (≈50 ppm CO_2) and ~800 cps for ^1H (0.03 wt% H_2O). We calibrated H_2O and CO_2 against synthetic basaltic glass standards (Lesne et al., 2011) containing 0 to 3 wt% H_2O and 0 to 2000 ppm CO_2. Calibration working curves of $^1H/^{30}Si$ vs H_2O and $^{12}C/^{30}Si$ vs CO_2, used to calculate H_2O and CO_2 content, gave straight lines with $R^2 \geq 0.99$.

3.3. Raman spectroscopy

Raman spectra were obtained at MSU using a JY Horiba XPloRA Jobin confocal Raman microscope attached to an Olympus BX41 polarizing microscope equipped with two lasers (532

and 785 nm). The operating temperature of the CCD (IVAC Andor CCD) detector is -51 °C, cooled by Peltier elements. Spectra accumulation was performed at excitation by the 532 nm laser at a power of 25 mW, 100x magnification (spatial resolution of <1 µm), a spectrometer slit of 100 µm, and a confocal hole of 300 µm. Spectra were acquired in the range 100 to 4000 cm^{-1} using an 1800T spectral grating. The accumulation time of each spectral window was 120 seconds (3 x 40 seconds). Initial processing of the spectra was carried out using LabSpec, ver. 5.78.24. We used a linear correlation between the content of water in the glass and the ratio of the O-H and 800-1200 cm^{-1} vibrational band areas (Rw/Rs ratio) for measurement of water content (Le Losq et al., 2012). Quantitative determination of water in glass relative to Rw/Rs is correct if the standard glasses are similar in NBO/T to the measured samples. Glasses of melt inclusions in olivine, which are described in this paper, have NBO/T in the range 0.07-0.1. We used as primary standards synthetic glasses with NBO/T=0.2 and water contents of 0-6.7 wt. % (Shishkina et al., 2010). H_2O contents of inclusions analysed by both Raman and SIMS are in good agreement (Figure 2) except for the two largest inclusions where we speculate that the difference is due to glass inhomogeneity.

3.4. Whole rock analyses

Twenty-one whole rock samples were analysed for major elements by X-ray fluorescence (XRF) at ETH-Zürich. The BCR-2 basaltic standard was used for quality control. Three of our samples were also analyzed by XRF in IGEM RAS, Moscow, to compare with published data for the 2012-13 eruption from Volynets et al. (2013) and Zelenski et al. (2014) analyzed previously at IGEM. Standard deviation of ETH analyses lies within 0.65 rel.% for all major elements except MnO (4 rel. %). Standard deviations for same samples produced in IGEM exceed 1 rel.% for Al_2O_3, FeO^{tot}, MgO, Na_2O and P_2O_5 but lie within 5 rel.%. We found significant systematic differences between analytic results of the two laboratories in contents of Al_2O_3 (4 rel.%), FeO^{tot} (0.4 rel.%), MgO (7.6 rel.%), CaO (0.8 rel.%), Na_2O (2.7 rel.%), K_2O (0.5 rel.%). We recalculated previously published analyses for inter-laboratory difference for correct comparison in plots.

3.5. Electron microprobe analyses (EPMA)

Melt inclusions were analysed for major elements using a Cameca SX100 microprobe at the University of Bristol. Major element composition was calibrated on oxide and silicate standards. To minimize alkali loss during hydrous glass analysis we used 4 nA probe current and 10 µm spot size. Cl and S were analysed separately and calibrated on NaCl and barite respectively. We followed the method of Sobolev et al (2007) to obtain high-precision olivine analyses by using a

JEOL JXA-8230 microprobe at MSU. We used San-Carlos olivine USNM-111312/444 as a primary standard for Si, Mg, Fe, oxides for Ti, Mn, Cr, Al, Ni, wollastonite for Ca and apatite for P. Images of typical olivine-hosted melt inclusions are given in Figure 3.

Back-scattered electron (BSE) images were obtained on a JEOL JSM-6480 scanning electron microscope (MSU). Rock porosity and crystallinity were calculated from BSE images and ImageJ software. We used 10-15 BSE images with two different scalings for each sample. 5 different phases (olivine, plagioclase, titanomagnetite, glass and vapour) were determined by BSE contrast. Shallow vapour bubbles (not filled by epoxy resin) were shadowed manually. For recalculation from volume to mass proportions we used the following densities (kg/m^3): olivine – 3300, plagioclase - 2690, titanomagnetite – 5300, glass – 2500, vesicles – 0.

4. Petrology and geochemistry

4.1. Bulk rock geochemistry

Bulk rock major element compositions for all samples are presented in Table 2. All Tolbachik 2012-13 lavas fall into the basaltic trachyandesite field (Figure 4a), which can be divided further into mugearites and shoshonites (Le Maitre et al., 2002). Both MGV and NGV lavas are well above the discrimination line (Na_2O-2 = K_2O) and should therefore be classified as shoshonites in the UIGG classification scheme (Le Maitre et al., 2002). Tolbachik 2012-13 lavas lie on the boundary between high-K and shoshonitic fields in the SiO_2-K_2O discrimination diagram (Figure 4b). Most classical Hawaiian mugearites have similar or higher K_2O content, suggesting that SiO_2-K_2O alone cannot be used for discrimination between shoshonites and mugearites. Thus, the Tolbachik 2012-13 eruption is the first known Holocene (or even Quaternary) evidence of shoshonite lava in Kamchatka.

Lavas of MGV are characterized by higher silica content (up to 55.7 wt%) and alkalis, but less MgO than NGV lavas (Figure 4). Lavas of NGV have very homogenous compositions at least since January 2013 (see Table 1 and Figure 2). NGV lavas from the Toludskoe and Leningradskoe lava fields have the same composition (within analytical error).

4.2. Petrography and mineralogy of MGV and NGV vents

We studied the mineralogy and petrology of both MGV and NGV samples and melt inclusions in olivine from NGV. All rocks are almost aphyric with very rare phenocrysts of olivine and plagioclase. Representative mineral analyses are provide in Table 3.

4.2.1 Menyailov group of vents (MGV).

We have only one sample of lava from MGV (Table1). These lava blocks were collected by V.M. Okrugin close to the vent in December 2012. This sample has a very heterogeneous texture (Figure 5a) with three distinct components in terms of 1) porosity and bubble size; 2) groundmass crystallinity; and 3) transparency in thin section. BSE images of the macroscopic textures of three different components of the MGV sample are shown in Figure 5a-c; their groundmass textures in Figures 5d-f. Typical mineral textures are shown in Figure 6.

High-porosity areas (porosity about 35%) have sharp contacts against the surrounding rock (Figure 5a,b). They contain numerous olivine and clinopyroxene microphenocrysts in equal proportion set in a groundmass (Figure 5d) consisting of plagioclase microlites (An_{70-71}) and very fine (much less than 1 μm) aggregates of minerals. Clinopyroxene shows very complex zoning of both sectoral and oscillatory varieties (Figure 6a,b). Compositions of cores (sectoral and oscillatory) lie in the narrow range of Mg#[1] – 89-90.5. The thin outermost rim of each grain has Mg# of about 83. Olivine also shows oscillatory zoning in the cores of grains (Fo_{85-86}) whereas the outermost rim has much more Fe-rich composition ($Fo_{72.1}$) evident as a bright rim in BSE images (Figure 6b). There is no clear evidence of dissolution of these phenocrysts.

Porous areas (porosity = about 10%) have more coarsely crystallized groundmass than high-porosity areas (Figure 5c,e). Rare plagioclase phenocrysts (An_{63-78}) aggregate into small clots with clinopyroxene (Mg# = 82 mol.%) (Figure 6d). Porous areas look darker in transmitted light than the surrounding low-porosity area and contain relatively large bubbles (up to 1 mm). Groundmass consists of plagioclase microlites (An_{56-61}), clinopyroxene and oxides. Glass patches are too small to analyze.

Low-porosity areas (Figure 5f) contain almost no bubbles (porosity ≤ 1%). Only one group of plagioclase phenocrysts (up to 1 mm in length) occurs in these areas. The large plagioclases have both oscillatory and sectoral zoning (Figure 6c). Anorthite content varies in the range 67-77 mol.%. The outermost rim (An_{57}) shows skeletal growth forms. One of these crystals (uppermost in Figure 6c) appears crushed and then overgrown by a rim, suggestive of a xenocrystic origin. Low-porosity areas are lighter than other components of the rock and contain about 15% interstitial glass. Plagioclase microlites (An_{54}) grew up to 100 μm and form fluidal microstructures (Figure 6c). Clinopyroxene and oxide mineral grains are much smaller and occupy interstitial space. Olivine has a skeletal morphology; cores contain up to 76 mol.% Fo; skeletal parts are $Fo_{66-67.4}$. Skeletal olivine also contain up to 0.46 wt.% P_2O_5 (Table 3).

[1] Mg# = 100* molar $Mg/(Mg+Fe^{2+})$

We interpret this MGV rock as an autobreccia, where a crystallized and vesiculated crust was crushed by and incorporated into subsequent portions of lava. Based upon inclusions relationships the earliest portion is represented by the high-porosity areas, then the porous areas solidified or almost solidified. The surrounding low-porosity component, containing significant glass, is thought to represent the youngest, liquid part of the lava. These textural relationships suggest incorporation of fragment of older magma into the present eruption. It is unclear whether the older fragments pre-date significantly the 2012-13 eruption although their fluidal textures and lack of reaction rims (Figure 5b) suggest that they are not vestiges of the 1975-76 eruption.

4.2.2 Naboko group of vents (NGV)

Three samples were selected for detailed petrographic study. The first is pieces of air-collected tephra (PK-13/4b; Figure 1b), the second comes from the moving lava front, hot-collected in the liquid state and quenched (PK-13/7; Figure 1c), and the last is naturally solidified "toothpaste" lava from the western branch of the Toludskoe lava field (PK-13/6). All three samples have very similar bulk composition, within analytical error, but the structures of their groundmass are markedly different (Figure 7). All three samples were collected within 2 days of each other in early August 2013 and we can assume that initial lava was identical for all of them. Representative mineral analyses are given in Table 3.

Tephra pieces are very porous (average porosity is 53 vol. %). Bubbles, up to several millimeters across, have complex elongated shape. Groundmass between bubbles consists of glass (69-77 vol. %) and microlites of plagioclase (An_{55-64}), olivine (Fo_{67-68}) and titanomagnetite (Figure 7a). Lava from the active lava front (Figure 7b) is much less porous (average = 6 vol. %). Groundmass of hot-collected sample is glassy (71-77 vol. %), whereas groundmass in naturally solidified sample is finely crystallized with dendritic crystals (Figure 7c). Plagioclase (An_{54-64}), olivine (Fo_{67-69}) and titanomagnetite are in the same proportions and have very similar composition compared to tephra. Olivine phenocrysts have a high 75-69 mol. % of Fo. Large plagioclase crystals in the slowly-cooled lava (sample PK-13/6) show zoning in the range of 67-79 mol. % of An.

4.3. Mineral chemistry and evolution

Olivine and plagioclase are the dominant phases in all varieties of 2012-13 eruptive products. Clinopyroxene phenocrysts are only found in MGV sample Tolb2012. The most magnesian olivine (Fo_{85-86}) and clinopyroxene (Mg#-89-90.5) compositions are typical for high-porosity

areas in lavas of MGV (Figure 8, Table 3). In this rock plagioclase is present only as microlites together with olivine, clinopyroxene and Fe-Ti oxides. The phenocryst assemblage of low-porosity areas of MGV lavas and NGV tephras and lavas is similar and consists of olivine ($Fo_{72.2-75.8}$), plagioclase (An_{77-78}) and clinopyroxene (Mg# 80.3-83). The only difference is the absence of clinopyroxene as separate phenocrysts in NGV eruptive products; it is present only as mineral inclusion in olivine crystals and as microlites. Based on mineral chemistry all rock varieties may be considered to be derived from the same magma without evidence of magma mixing, other than incorporation of autobrecciated fragments, described above from MGV.

4.3.1 Clinopyroxene

Clinopyroxene is rare in our samples, occurring in 3 morphological types: 1) inclusions in olivine, 2) phenocrysts-microphenocrysts and 3) microlites. Clinopyroxene phenocrysts, up to 0.5 mm, are found in MGV lavas only (most abundantly in high-porosity areas). Phenocryst cores have complex rhythmic zoning with Mg# varying from 89.1 to 90.5 mol.%. Phenocrysts rims have Mg# about 83 mol.%. Low-porosity areas contain rare clinopyroxene microphenocrysts with size about 300 µm. The Mg# of microphenocrysts is about 82 mol.%. NGV lava and tephra contains clinopyroxene inclusions in olivine phenocrysts and in the finely crystallized groundmass. Included crystals are euhedral, up to 100 µm in size, and typically show complex sectoral zoning. Their Mg# varies from 77.2 to 81.8 and is comparable with clinopyroxene microphenocrysts of MGV low-porosity areas. The finely crystallized groundmass assemblage in PK-13-6 contains dendritic clinopyroxene crystals up to 20-30 µm in length with Mg# of 74-78.5.

4.3.2 Plagioclase

We observed four plagioclase morphology types: 1) inclusions in olivine phenocrysts, 2) phenocrysts, 3) microphenocrysts and 4) microlites. Plagioclase inclusions vary in size from 40 to 70 µm. They have euhedral, lath-like shapes and are homogeneous in composition (An_{77-80}). Host olivine varies from Fo_{73} to $Fo_{74.5}$ (average $Fo_{73.5}$). Plagioclase phenocrysts, up to 2 mm across, occur in all NGV samples and in low-porosity areas of the MGV sample. The phenocrysts have complex zoning and An content lies in range 56-78 mol.%. An-rich phenocryst cores correspond in composition to the olivine-hosted inclusions, suggesting that they grew at the same time. Microphenocrysts (size less than 300 µm) show simple normal zoning, with uniform composition cores (An_{63-64}), whereas rims vary in the range An_{55-59} for the near-vent sample (PK-13/4b) and An_{54-57} for the lava front sample (PK-13/7). Rims of both phenocrysts and microphenocrysts have very similar composition and texture. Microlite, up to 100 µm,

compositions in MGV lavas are different in different areas. High-porosity areas contain microlites of An_{70-71}, porous areas - An_{56-61} and low-porosity areas - An_{54-55}. Microlites in NGV lavas and tephra are An_{54-57}.

4.3.3 Spinel

Spinel shows a discontinuous change in composition from Cr-spinel to titanomagnetite (Figure 9). Cr-spinel was found only as small (5-10 µm) inclusions in olivine in high-porosity areas of the MGV sample. Titanomagnetite occurs in a variety of forms: euhedral microphenocrysts (100-300 µm), small individual grains (1-10 µm) and as chains of 20-30 grains. The decrease of spinel Al_2O_3 abundance (Figure 9d) reflects a change of melt composition with progressing fractional crystallization, however Al_2O_3 vs TiO_2 shows a negative correlation (Figure 9e).

The mineral chemistry in different MGV textural varieties and NGV magmas is summarized in Figure 10.

4.4. Groundmass glasses

We measured groundmass glass compositions in all types of samples (Table 4). In general glasses have shoshonitic composition with Mg# 36-37 mol.%, high K_2O (2.8-3.1 wt.%), high TiO_2 (2.2-2.5 wt.%) and high P_2O_5 (1.0-1.2 wt.%). Despite similar bulk compositions interstitial glasses in near-vent tephra and hot-collected lava front samples are slightly different. Those from the lava front are slightly depleted, compared to near-vent glasses, in MgO, FeOt and Al_2O_3 and enriched in SiO_2, K_2O, TiO_2 and other incompatible elements, consistent with small amounts of crystallisation (see section 5).

5. Chemical and physical changes during lava flow

Our sampling strategy and petrological observations allow us to quantify changes that take place along the flow path of the lava from the NGV vent (PK-13/4b) to the lava fields, as represented by both the hot-collected lava sample (PK-13/7), and from older, solidified portions of the Toludskoe lava field (PK-13/6). The associated changes in groundmass texture are shown in Figure 7. For the purposes of comparison we will assume the same initial magma composition for volcanic bombs sampled near the vent and lavas elsewhere on the Toludskoe lava field. This assumption is justified on the basis of the chemical and petrologic data presented above. The modal proportions and calculated physical properties of the three samples are given in Table 5.

The site of hot-collected lava lies 5.25 km from the vent (Figure 1a) down a slope of approximately 7.5°. Thus, samples PK-13/4b and PK-13/7 are related to each other by time spent in the lava flow, with little cooling en route. This is consistent with the flow lying mostly beneath an insulating crust of solid lava (Figure 1c). Conversely, PK-13/4b and PK-13/6 are related by significant cooling and solidification. PK-13/4b and PK-13/7 have almost identical crystallinity and mineral proportions (within uncertainty) indicative of negligible crystallization during flow. However, there is significant reduction in porosity during flow from 54% to 6% due to degassing, consistent with extensive gas discharge through skylights and other cracks in the crust of the flowing lava. Upon solidification the porosity increases slightly (to 8%), probably due to exsolution of further volatiles from the melt as groundmass microlites form. On solidification there is significant increase in crystallinity from 26 to 43%. There is a steady reduction in the ratio of olivine to plagioclase crystallising, from more than 10 in the pyroclastic sample; to 8 in the liquid lava front; to 4.5 in the naturally solidified lava. The amount of oxide mineral also increased from 0.5 vol.% near the vent, through 0.8 vol.% at the liquid lava front, to 1.9 vol.% in the solidified lava. Interestingly the reduction in porosity, with little net change in crystallinity or temperature, leads to a reduction in calculated effective viscosity by about 0.5 $\log_{10}$ units during flow (Table 5).

We can calculate the amount and proportion of minerals crystallizing during the flow of the lava from NGV to the hot-sampling site if, as proposed above, we assume that the composition of crystallizing minerals does not change significantly during flow. In order to perform these calculations microphenocryst compositions for olivine, plagioclase and magnetite in sample PK-14/7 were averaged (Table 6). For each element, *i*, a mass-balance equation for the proportion, *C*, of each mineral, with composition *X*, was written as $C_0 * X^i_{Tephra-gl} - C_1 * X^i_{ol} - C_2 * X^i_{Pl} - C_3 * X^i_{Mt} = X^i_{Lava-gl}$. The amount of crystallizing minerals was obtained by least squares for differences between calculated and measured composition of glass in the lava-front sample (Table 6). The best fit is achieved with crystallization of 1 wt.% of olivine, 5.3 wt.% of plagioclase and 0.6 wt. % titanomagnetite during surface lava flow. The total amount of crystallization is estimated as 6.9 wt.% (6.5 vol.%). This value is slightly greater that the change in crystallinity estimated from BSE images (Table 5) and may reflect the limitations of our assumptions that vent tephra and hot-collected lava were initially identical. Regardless, it is clear that very little crystallization occurred during flow from vent to lava front. We note that the calculated amount of crystallized plagioclase is 5 times more than amount of olivine. A possible explanation is the evident degassing of lava during flow (reduced porosity), which will expand the plagioclase crystallization field. Interstitial groundmass glass compositions will be discussed

in comparison with MI compositions in section 6. We were not able to perform similar mass balance calculations for the naturally solidified lava (PK-13/6) because the interstitial glass pools were too small to analyse.

6. Melt Inclusions

Melt inclusion major element compositions were analysed in two rapidly-cooled tephras (NK-13/2 and NK-13/3), hot-collected lava (PK-13/7) and slowly-cooled, solid lava (PK-13/6), and a reheated set of MI from NK-13/2. Volatile contents were analysed (by SIMS and Raman) in all MI, with the exception of PK-13/7 (by Raman only). Groundmass glasses were analysed for major elements in the different textural components of MGV sample, and in PK-13/4b and PK-13/7. Groundmass glass volatile analysis was only possible in the tephras (Table 7). All original melt inclusion glass analyses, including volatiles and host olivine Fo contents are given in Table 7. H_2O contents range from 0.1 to 1.6 wt.%; CO_2 range from 88 to 883 ppm. Sulphur contents are consistently low, 100-630 ppm S; chlorine lies in the range 220-870 ppm. Host olivines are relatively homogeneous with Fo from 70 to76 mol.%.

6.1. Major Element Melt compositions

Melt inclusion compositions were reconstructed to remove the effects of any post-entrapment re-equilibration using the method described in Supplementary Information. The reconstructed major element compositions, used for all subsequent plots, are given in Table S1. Reconstructed MI compositions lie remarkably close to bulk rocks (Figure 11). This indicates that (a) bulk rocks are representative of true liquid compositions with negligible addition of xenocryst or antecrysts and (b) that these magmas did not undergo significant crystal fractionation during magma ascent and solidification. Moreover, MI were not affected by any irreversible post-entrapment changes in major element chemistry and can be used for magma condition reconstructions. However, as we will show in section 6.3, there is evidence of volatile loss from the slowly-cooled inclusions and this must be taken into account when attempting to reconstruct pre-eruptive volatile budgets.

As expected, the groundmass glasses from MGV samples are displaced from bulk rock and melt trends (Figure 11). The displacement is relatively small for those samples from the high porosity areas, but is significant for low porosity areas. This is consistent with our interpretation that the high-porosity areas represent samples of rapidly cooled lava crust incorporated into low-porosity lavas that have undergone significant groundmass crystallization during cooling. The groundmass glasses from NGV samples are also displaced from the bulk rock and melt trends,

again due to subsequent crystallization of groundmass minerals. The displacement is slightly greater for the hot-collected lava front samples in keeping with their higher crystallinity. For some elements, e.g. K_2O, CaO, the NGV groundmass glasses are collinear with the melts and the MGV groundmass glasses, whereas for others (TiO_2, P_2O_5) there is a marked inflexion between the two, reflecting the onset of groundmass magnetite (with 1-14 wt % TiO_2; Figure 9e) and apatite crystallization, respectively, below Mg# = 33.

6.2 Geothermometry and oxybarometry

Magma crystallization temperature estimated by olivine-melt equilibrium accounting for the measured dissolved water contents of the melts (Danyushevsky, 2001) is in the range 1040-1080°C (Table S1). The same olivine-melt equilibrium equations using different coefficients suggested for higher water content (Almeev et al., 2007) yields slightly higher temperatures of 1081-1115°C. Clinopyroxene-olivine equilibrium in high-porosity areas of MGV sample Tolb2012 gives 1121±15°C (Loucks, 1996) and olivine-spinel equilibrium temperature in the same sample is near 1080°C (Ballhaus et al., 1991). These temperatures correspond well to direct field measurements of the lava flow, ≤1080°C (Edwards et al., 2014) and MI homogenization temperatures (section 3.1). We conclude that the pre-eruptive magma temperature was 1080-1120°C and the temperature of lava at the moment of eruption was about 1080°C.

Oxygen fugacity, estimated by olivine-spinel equilibrium (Ballhaus et al., 1991), for Tolb2012 sample lies between NNO and NNO+1 log units. Also we estimated oxygen fugacity in the sample PK-13-4b by equilibrium between olivine and quenched glass (Ford et al., 1983) and it also corresponds to NNO.

6.3 Volatile content of melt inclusions

Relatively few melt inclusions in olivine from tephra have gas bubbles and many inclusions lack shrinkage bubbles. The size of gas bubbles in these inclusions is up to 4.3 vol.%. There is no systematic difference in volatile content between inclusions with or without gas bubble. We interpret this lack of difference to be due to heterogeneous entrapment of melt and bubble, rather than post-entrapment vesiculation, which would modify the volatile contents of those inclusions. The amount of correction required to account for post-entrapment crystallization is relatively small: <3% for tephra and lava, 1-4% for heated inclusions, and 5-8% for slowly-cooled lava (Table S1). These corrections primarily affect MgO and FeO contents; their effect on measured volatile contents is small compared to the overall variability and to the analytical precision.

Consequently will discuss volatile contents in terms of the original measured values given in Table 7.

Melt inclusions from tephras and re-heated olivines are remarkably similar in composition. They define a ten-fold range in CO_2 (90-900 ppm) at near constant H_2O (1.19±0.14 wt%, with the exception of two low-H_2O outliers). This is consistent with a simple degassing trend with limited concomitant crystallisation (Blundy and Cashman, 2008; Figure 12a). For these MI there is a crude positive correlation between S and H_2O (Figure 12b), with the lowest S contents at lowest H_2O (and CO_2), consistent with sulphur degassing, although the three highest CO_2 MI and the two highest sulphur MI are unexplained outliers to this trend. The sulphur contents of 2012-13 MI are considerably lower than those from other Kluchevskoy Group magmas (Figure 12b). Chlorine does not correlate obviously with H_2O (or CO_2) and lies at the lower end of MI from other Kluchevskoy Group magmas (Figure 12c). Groundmass glasses from the tephra sample have low H_2O (0.3 wt%) and CO_2 (50 ppm) consistent with continued degassing. These glasses lie at the low pressure continuation of the degassing trend defined by the tephra and hot-collected lava. One tephra MI with low H_2O (0.45 wt%) and low CO_2 (88 ppm) also lies on the same degassing trend, possibly consistent with degassing and olivine crystallisation at the vent itself. There is a slight negative correlation between K_2O and CO_2 consistent with a small amount of crystallization occurring during degassing. This relationship is explored quantitatively in section 6.4.

We have several reasons to believe that the measured H_2O content of MI from tephra represent original magmatic values. Firstly, we used olivine-hosted MIs from ash-sized (0.5-1 mm) tephra only for volatile content reconstructions. Effect of tephra particle size (Lloyd et al., 2013) for these MIs should be negligible. Secondly, as melt inclusion H_2O loss leads to oxidation and crystallization (e.g. Sobolev & Chaussidon, 1996; Danyushevsky et al., 2002; Portnyagin et al., 2008; Lloyd et al., 2013), any significant water-loss processes should be followed by pressure drop, bubble formation and host mineral crystallization. Most of the studied MIs lack shrinkage bubble. A few inclusions have bubbles up to 4.3 vol.%, but there is no systematic difference in volatile contents between inclusions with or without bubbles. Finally, estimated post-entrapment crystallization in MIs does not exceed 2-3 wt. % (equivalent of 20-40 °C cooling) consistent with magma cooling during ascent and any brief residence in the small NGV lava lake prior to eruption. Furthermore, we do not observe diffusion profiles in olivine around any MIs precluding any significant re-equilibration via iron-loss. Consequently, the FeO content of MIs corrected for host olivine crystallization corresponds to whole-rock values (Figure S1).

In contrast MI from the slowly-cooled lava sample (PK-13/6) show a similar range in CO_2 (100-700 ppm), S and Cl, but much lower H_2O (0.13±0.03 wt%). The hot-collected lava sample (PK-13/7) has H_2O contents below the Raman detection limit of ~0.1 wt%; we have no SIMS H_2O or CO_2 data for these MI. At first sight the low H_2O/high-CO_2 contents of MI from PK-13/6 (and, by inference, PK-13/7) are also reminiscent of a degassing trend starting at very low H_2O. However, given the abundant evidence that the slowly-cooled lavas, hot-collected lava and tephras originate from the same magma, it seems unlikely that a batch of this magma could have had a ten-fold lower initial H_2O content. Instead it seems much more likely that during slow cooling H_2O was lost from melt inclusions (e.g. Lloyd et al, 2013). This may occur via cracks linking the MI to the matrix, or via diffusion across the host olivine. The similarity in contents of other volatile elements (S, Cl) between the two populations suggests that diffusion through olivine is the key process.

Several recent experimental studies (Portnyagin et al. 2008; Gaetani et al. 2012; Bucholz et al., 2013) have shown that H_2O loss by diffusion through olivine occurs on timescales of hours at temperatures of 1100 °C. The driving force for diffusion in these experiments is the contrast in H_2O partial pressure (fugacity) between the inclusion and the atmosphere. Gaetani et al (2012) proposed a novel mechanism for H_2O loss that does not require oxidation of the melt inclusion, consistent with our observation that MI in the H_2O-depleted, slowly-cooled lava lack magnetite microlites. The loss of H_2O from the hot-collected lava suggests that diffusion occurred during the time taken for the lava to flow from the vent to the hot-collection site. This timescale is hard to constrain from our field observations because the lava flow velocities across the entire thickness of the flow are not easily estimated. Within the lava tube (Figure 1c) the surface flow velocity was estimated in the field as 2-3 m/s. This gives a minimum travel time to the collection site 5.25 km away as 40-60 minutes. This is likely a gross under-estimate because deeper portion of the flow will flow more slowly. Gaetani et al (2012) and Bucholz et al (2013) show that H_2O loss at 1100 °C, the same temperature as Tolbachik lavas, is around 50% after only 4 hours, thus flow times of the order several hours are consistent with the low H_2O from MI in hot-collected lava. A single tephra MI with low H_2O (0.54 wt%), but elevated CO_2 (256 ppm) also appears to have lost H_2O, as it is displaced from the degassing trend in Figure 13a. Perhaps this MI lost H_2O after spending a few hours at the surface of the small lava lakes at NGV prior to expulsion as tephra. The rest of the tephra MI do not appear to have lost H_2O at this stage.

It is striking that there is no loss in CO_2 or S from MI in the slowly-cooled lava. The experiments of Bucholz et al. (2013) indicate that H_2O, CO_2 and S are lost from MI at approximately the same rate. However, CO_2 diffuses through olivine much more slowly than H_2O, regardless of the

exact mechanism, primarily because C solubility in olivine is so low (Bucholz et al, 2013). Thus Bucholz et al (2013) propose that the mechanism for CO_2 reduction in their experimental MI is through exsolution into a tiny vapour bubble, occasioned by the pressure drop resulting from H_2O loss. This explanation for the experimental data is entirely consistent with our own observation that the MI we have studied contain negligible or no shrinkage bubbles (Figure 3) and reinforces our assertion (see below) that those bubbles that we do see were co-entrapped with the melt. Our findings reiterate the perils of measuring H_2O contents of olivine-hosted MI in anything other than very rapidly cooled, small tephra (Lloyd et al, 2013); more slowly cooled or larger samples are very likely to have suffered H_2O loss.

6.4. Pre-eruptive magma storage conditions

Having established that MI from tephras preserve their original volatile contents, we can calculate trapping pressures using volatile solubility relationships. To do this requires that the melt inclusions were volatile-saturated at the time of entrapment. There are two observations in support of this. Firstly, we argue that rare, small vapour bubbles in some MI were co-entrapped with melt. Secondly, the overall variation in MI chemistry, namely a wide range in CO_2 at near-constant H_2O, is consistent with a degassing trend. In fact the degassing trend In Figure 13a is refreshingly free from many of the complexities often seen in MI from basaltic eruptions, variously attributed to variable H_2O loss or CO_2-rich volatile fluxing (Blundy & Cashman, 2008).

We have calculated volatile saturation pressures (Table 7) for MI with analyses of both H_2O and CO_2 at the olivine-melt temperatures given in Table S1 using the basalt algorithm of Newman & Lowenstern (2002) with SiO_2 set at 49 wt%. The overall spread in pressure is from 1.94 to 0.15 kbar (Figure 13a). Taking a mean density for the basaltic crust of Kamchatka of 2.69 g/cm^3 (Frolova et al., 2014) this pressure range corresponds to depths from 0.6 to 7.5 km below the surface. These data compare favourably to the location of a swarm of magnitude 1 to 2.25 earthquakes that occurred beneath the south flank of Ploskii Tolbachik on 26th November 2012 at depths of 1 to 5 km below sea-level, or 3 to 7 km below the 2012-13 vents (Senyukov et al., 2013). These events probably record activity along a dyke or conduit supplying magma to the surface, and so represent depth estimates for the uppermost levels of the magma reservoir.

We can calculate the amount of degassing-driven crystallization that occurred during ascent by taking the calculated volatile saturation pressure and the K_2O content of each MI as an indicator of the degree of crystallization, assuming that K is a completely incompatible element. To do this we take as our starting composition the minimum K_2O of the NGV bulk rock, 2.35 wt% (Table

2). Thus crystal fraction is given as $1 - \left({}^{2.35}/_{\mathrm{K_2O^{MI}}}\right)$. Results of these calculations are given in Figure 12d and indicate no more than 15 wt% crystallization occurred during ascent from 1.9 to 0.2 kbar. The groundmass glass from the tephra is consistent with a further 2-3% crystallization during the final ascent. The relatively limited amount of crystallisation accompanying ascent suggests that magmas ascended rapidly from a magma chamber, at around 7 km depth, to the surface during eruption, pausing only briefly in vent lava lakes.

7. Petrogenetic relationships between products of the 2012-13 and 1975-76 eruptions

7.1 Comparative petrology and geochemistry

It is instructive to draw some comparisons between the petrology and geochemistry of the 2012-13 and 1975-76 lavas. The mineral chemistry of the 2012-13 lavas is summarised in Figure 10; bulk-rock compositions from both eruptions are plotted in Figure 4. Petrologic data for the 1975-76 eruption are taken from Fedotov (1984).

The 2012-13 eruption has some common features with 1975-76. Both eruptions had two stages: a relatively short early stage from an upper vent and a longer stage from a lower elevation vent. The bulk compositions are different for upper and lower vents for both eruptions. For the 1975-76 eruption high-Mg basalts of the upper vent (North fissure) changed to high-Al trachybasalts from the lower vent (South fissure). The bulk-rock K_2O content increased from 0.9-1.3 wt.% in the early stage to 2-2.1 wt.% in the later stage of the eruption. For the 2012-13 eruption all bulk rock compositions lie within basaltic trachyandesite (shoshonite) field, but the earliest rocks (MGV) are less magnesian whereas the longer-duration, late-stage (NGV) rocks are more magnesian. In general, all lavas of the 2012-13 eruption have lower MgO and CaO content than any from the 1975-76 eruption. On the other hand 2012-13 lavas have systematically higher TiO_2 and alkalis (Figure 4).

During the 1975-76 eruption olivine-pyroxene phyric lavas changed to pyroxene-plagioclase-olivine-phyric lavas (upper vent) and then to plagioclase-phyric lavas (lower vent) containing plagioclase megacrysts up to 20-25 mm across. The 2012-13 eruptive products lack plagioclase megacrysts and only rarely (MGV) contain phenocrysts of clinopyroxene. Rare xenocrystic plagioclase megacrysts were observed in the 2012-13 products. Olivine and plagioclase compositions are very similar for both eruptions. For 1975-76 two populations of olivine were observed (Figure 8): $Fo_{85\text{-}90}$ (North fissure) and $Fo_{72\text{-}76}$ (South fissure), whereas the main olivine population of 2012-13 products is $Fo_{68\text{-}74}$. Plagioclase compositions from 1975-76 products are

An_{55-74}, whereas the main plagioclase population of the recent eruption is An_{54-64}. Cr-spinel from MGV is compositionally similar to Cr-spinel inclusions in olivine from 1975-76 (Figure 9).

7.2 Volatile contents

The fact that the MI lie on a degassing trend from higher to lower CO_2 indicates that the original melt did not have higher H_2O than the most H_2O-rich MI analysed, i.e. 1.45 wt.%, even if degassing began at much higher pressures (Blundy et al., 2010). For that reason we cannot, however, rule our appreciably higher original CO_2. Certainly the Tolbachik 2012-13 magmas are unusually poor in H_2O relative to other arc basalts where H_2O contents of 2 to 6 wt.% are more typical (Plank et al. 2013). The compilation of Plank et al. (2013) includes previously analysed MI from other Kamchatkan volcanoes, which range from 2.9 to 7.1 wt.%. Melt inclusions from other Kluchevskoy volcanoes (Auer et al, 2009; Portnyagin et al, 2007; Mironov and Portnyagin, 2011) have comparable CO_2 contents, but H_2O contents up to 4 wt% (Figure 13a). We do not yet have any measured H_2O or CO_2 contents from melt inclusions in the 1975-76 olivines. However, SIMS measurements of olivine-hosted MI from 1000-1500 yrs B.P. basaltic eruptions from Tolbachik reveal H_2O contents of 2.42±0.51 wt% (Portnyagin et al, 2007) suggestive of a drop in dissolved H_2O over that time period.

The low H_2O content of Tolbachik magmas is consistent with the relatively low An content of their plagioclases (An_{54-64}) and the early appearance of plagioclase relative to olivine on the liquidus, as evidenced by inclusions of plagioclase in olivine. It would appear that Tolbachik basalts and their derivatives are unusual in having low H_2O, but high K_2O. The low H_2O content, compared to other Kluchevskoy MI, cannot be attributed to further degassing of 2012-13 magma, because the range of CO_2 contents in both sets of MI is similar (Figure 13a). The unusual chemistry of Tolbachik 2012-13 magmas in H_2O-K_2O space is evident in Figure 13b, where it is seen that they have H_2O that is lower by a factor 2-4 to other Kluchevskoy Group magmas, but K_2O contents that are higher by a factor 2.5 to 4. A four- to five-fold increase in K_2O, an incompatible element, would require 75-80% crystallization, which is hard to reconcile with their basaltic trachyandesite composition. It is striking that other magmas erupted from the Kluchevskoy Group have significantly higher H_2O, despite being erupted only a few tens of kilometres to the north. In the absence of any MI volatile data from the 1975-76 Tolbachik eruption it is impossible to say when the apparent differences between Tolbachik and other Kluchevskoy magmas arose, nor what changes in magma storage depths occurred between 1975-76 and 2012-13. Further trace element and isotope geochemistry data, along with melt inclusions from 1976-76, are required to further explore possible petrogenetic links between the two most recent Tolbachik eruptions.

Acknowledgments

Fieldwork in Kamchatka was supported by a joint research grant from the Royal Society and the Russian Foundation for Basic Research (IE120094). Additional support to JB came from ERC Advanced grant CRITMAG. PP, NN and VS acknowledges partial support from M.V. Lomonosov Moscow State University Program of Development. We would like to thank O. Melnik, O. Dirksen, L. Porritt, K. Vlasov and D. Muir for assistance in the field, R. Hinton for help with SIMS analyses and A. Lloyd and G. Shellnut for constructive reviews.

References

Almeev, R. R., Holtz, F., Koepke, J., Parat, F., & Botcharnikov, R. E. (2007). The effect of H_2O on olivine crystallization in MORB: experimental calibration at 200 MPa. American Mineralogist, 92(4), 670-674.

Auer, S., Bindeman, I., Wallace, P.J., Ponomareva, V., Portnyagin, M., 2009. The origin of hydrous, high-$\partial^{18}O$ voluminous volcanism: diverse oxygen isotope values and high magmatic water contents within the volcanic record of Klyuchevskoy volcano, Kamchatka, Russia. Contrib. Mineral. Petrol. 157, 209–230

Ballhaus, C., Berry, R. F., & Green, D. H. (1991). High pressure experimental calibration of the olivine-orthopyroxene-spinel oxygen geobarometer: implications for the oxidation state of the upper mantle. Contributions to Mineralogy and Petrology, 107, 27-40.

Blundy, J., Cashman, K, Rust, A., Witham, F., 2010. A case for CO_2-rich arc magmas. *Earth and Planetary Science Letters* **290**, 289-301

Blundy, J**.,** Cashman, K., 2008. Petrologic reconstruction of magmatic system variables and processes. *Reviews in Mineralogy and Geochemistry*, **69**, 179-239.

Bucholz CE, Gaetani GA, Behn MD, Shimizu N (2013) Post-entrapment modification of volatiles and oxygen fugacity in olivine-hosted melt inclusions Earth and Planetary Science Letters 374, 145–155

Danyushevsky, L. V., & Plechov, P. (2011). Petrolog3: Integrated software for modeling crystallization processes. Geochemistry, Geophysics, Geosystems, 12(7).

Danyushevsky, L.V. (2001). The effect of small amounts of H_2O on crystallisation of mid-ocean ridge and backarc basin magmas. Journal of Volcanology and Geothermal Research, 110(3), 265-280.

Danyushevsky, L.V., McNeill, A.W., & Sobolev, A.V. (2002). Experimental and petrological studies of melt inclusions in phenocrysts from mantle-derived magmas: an overview of techniques, advantages and complications. Chemical Geology, 183(1), 5-24.

Dvigalo V. N., Svirid I. Yu., Shevchenko A. V. The first quantitative estimates of parameters for the Tolbachik fissure eruption of 2012–2013 from aerophotogrammetric observations// Journal of Volcanology and Seismology, 2014, Vol. 8, No. 5, pp. 261–268

Edwards, B. R., Belousov, A., & Belousova, M. (2014). Propagation style controls lava–snow interactions. Nature Communications, 5.

Edwards, B. R., Belousov, A., Belousova, M., Izbekov, P. E., Bindeman, I. N., Gordeev, E., ... & Melnikov, D. (2013, December). Lava-snow interactions at Tolbachik 2012-13 eruption: comparison to recent field observations and experiments. In AGU Fall Meeting Abstracts (Vol. 1, p. 02).

Fedotov S. A. (ed.) (1984) *The Great Tolbachik Fissure Eruption*. Znanie, Moscow, pp 637

Ford, C. E., Russell, D. G., Craven, J. A., & Fisk, M. R. (1983). Olivine-liquid equilibria: temperature, pressure and composition dependence of the crystal/liquid cation partition coefficients for Mg, Fe^{2+}, Ca and Mn. Journal of Petrology, 24(3), 256-266.

Frolova J., Ladygin V., Rychagov S., Zukhubaya D. (2014) Effects of hydrothermal alterations on physical and mechanical properties of rocks in the Kuril–Kamchatka island arc. *Engineering Geology* 183, 80–95

Gaetani, G.A., O'Leary, J.A., Shimizu, N., Bucholz, C.E., Newville, M. (2012). Rapid Re-equilibration of water and oxygen fugacity in olivine-hosted melt inclusions. Geology 40, 915–918.

Le Losq C., Neuville D. R., Moretti R., Roux J. Determination of water content in silicate glasses using Raman spectrometry: Implications for the study of explosive volcanism// Mineralogical Society of America, 2012 v. 97 no. 5-6 p. 779-790.

Le Maitre, R. W., Streckeisen A., Zanettin B., Le Bas M.J., Bonin B., Bateman P., Bellieni G., Dudek A., Efremova S., Keller J., Lameyre J., Sabine P.A.,Schmid R., Sørensen H., Woolley A.R. (2002). Igneous Rocks: A Classification and Glossary of Terms: A Classification and Glossary of Terms: Recommendations of the International Union of Geological Sciences, Subcommission on the Systematics of Igneous Rocks. Cambridge University Press, 236 p.

Lesne, P., Kohn, S., Blundy, J., Witham, F., Botcharnikov, R., Behrens, H., 2011. Experimental simulation of closed-system degassing in the system basalt-H_2O-CO_2-S-Cl. *Journal of Petrology* **52**: 1737-1762

Lloyd AS, Plank T, Ruprecht P, Hauri E, Rose W. (2013) Volatile loss from melt inclusions in pyroclasts of differing sizes. Contrib. Mineral. Petrol. 165, 129-153

Loucks, R.R. (1996). A precise olivine-augite Mg-Fe-exchange geothermometer. Contributions to Mineralogy and Petrology, 125(2-3), 140-150.

Mironov, N. L., Portnyagin, M. V. (2011). H2O and CO2 in parental magmas of Kliuchevskoi volcano inferred from study of melt and fluid inclusions in olivine. Russian Geology and Geophysics, 52(11), 1353-1367.

Mysen, B. O. (1983). The structure of silicate melts. Annual Review of Earth and Planetary Sciences, 11, 75-97.

Mysen, B. O. (1999). Structure and properties of magmatic liquids: From haplobasalt to haploandesite. Geochimica et Cosmochimica Acta, 63(1), 95-112.

Newman, S., & Lowenstern, J. B. (2002). VolatileCalc: a silicate melt–H2O–CO2 solution model written in Visual Basic for Excel. Computers & Geosciences, 28(5), 597-604.

Plank T, Kelley KA, Zimmer MM, Hauri EH, Wallace PJ (2013) Why do mafic arc magmas contain ~4 wt% water on average? Earth and Planetary Science Letters 364 168–179

Plechov P.Yu. Methods of melt and fluid inclusions study, KDU (Moscow), 2014, 266 p. (in Russian)

Portnyagin M., Almeev R., Matveev S., Holtz F.,2008, Experimental evidence for rapid water exchange between melt inclusions in olivine and host magma// Earth and Planet. Sci. Lett. 272, 541–552

Portnyagin, M., Hoernle, K., Plechov, P., Mironov, N., Khubunaya, S., 2007. Constraints on mantle melting and composition and nature of slab components in volcanic arcs from volatiles (H_2O, S, Cl, F) and trace elements in melt inclusions from the Kamchatka Arc. Earth Planet. Sci. Lett. 255, 53–69

Samoylenko S.B., Melnikov D.V., Magus'kin M.A., Ovsyannikov A.A. Beginning of new fissure Tolbachik eruption in 2012// Herald of KRAUNC, Earth Sci., 2012, N.2, issue 20, pp. 20-22 (in Russian).

Senyukov, S. L., Nuzdina, I. N., Droznina, S. Y., Garbuzova, V. T., Kozhevnikova, T. Y., Sobolevskaya, O. V., Bliznetsov, V. E. (2015). Seismic monitoring of the Plosky Tolbachik eruption in 2012–2013 (Kamchatka Peninsula Russia). Journal of Volcanology and Geothermal Research, this volume

Shishkina, T. A., Botcharnikov, R. E., Holtz, F., Almeev, R. R., & Portnyagin, M. V. (2010). Solubility of H_2O and CO_2-bearing fluids in tholeiitic basalts at pressures up to 500MPa. Chemical Geology, 277(1), 115-125.

Sobolev, A. V., Hofmann A.W., Kuzmin D.V., Yaxley G.M., Arndt N.T., Chung S-L, Danyushevsky L.V. et al. (2007) The amount of recycled crust in sources of mantle-derived melts. Science 316, 5823: 412-417

Sobolev, A. V., & Chaussidon, M. (1996). H_2O concentrations in primary melts from supra-subduction zones and mid-ocean ridges: Implications for H2O storage and recycling in the mantle. Earth and Planetary Science Letters, 137(1), 45-55.

Volynets, A. O., Melnikov, D. V., & Yakushev, A. I. (2013). First data on composition of the volcanic rocks of the IVS 50th anniversary Fissure Tolbachik eruption (Kamchatka). Doklady Earth Sciences, Vol. 452, No. 1, pp. 953-957.

Zelenski, M., Malik, N., Taran, Y. (2014). Emissions of trace elements during the 2012–2013 effusive eruption of Tolbachik volcano, Kamchatka: enrichment factors, partition coefficients and aerosol contribution. Journal of Volcanology and Geothermal Research, 285, 136-149.

Figure Captions

Figure 1. A - Schematic areal distribution of Tolbachik 2012-13 lava flows and sample locations. Eruptive vents are marked by stars. MGV – Menyailov group of vents, NGV – Naboko group of vents. The three lava fields described in the text are labeled. B – explosions in one of the NGV. C – skylight into subterranean lava flow. Lava is flowing at approximately 1-2 m/s and discharging significant quantities of gas. D – hot-collecting of samples from the active lava front. E – morphology of NGV lava front, showing individual lobes.

Figure 2. Comparison of melt inclusion H_2O analyses by Raman spectroscopy and SIMS. Solid line (1:1) marked the equal amounts of water measured by two methods.

Figure 3. Photos of representative primary glassy melt inclusions in olivine. a – b – naturally quenched melt inclusions in olivine grains from hot-collected lava front sample PK-13/7. c. Melt inclusion from PK-13/7 prior to reheating experiment. d – Melt inclusion from tephra sample NK-13/3 prior to reheating experiment. Note presence in c and d of a single large bubble, but lack of any small, shrinkage bubbles around the inclusion margins. e – melt inclusion from NK-13/3 after reheating experiment. f. melt inclusion from tephra sample NK-13/2 after reheating experiment showing ripple surface formed during heating.

Figure 4. Chemical classification diagrams for Tolbachik volcanic rocks from 2012-13 compared to previous Tolbachik eruptions. A) Total alkalis-silica (TAS) diagram for lavas. B) K_2O vs SiO_2 diagram. NGV lava analyses from Volynets et al. (2013); Zelensky et al. (2013); this study), MGV lavas (Volynets et al., 2013), 1975-76 eruption and older Tolbachik lavas from Georoc database. Discrimination fields are from Le Maitre et al. (2002).

Figure 5. Heterogeneity in MGV sample Tol-12/1 showing the distinct textures described in the text. A - overview of thin section showing high-porosity area (outlines in yellow); B - Contact of high-porosity and low-porosity areas; C - contact of porous and low-porosity areas. D - structure of groundmass in high-porosity area (we show an area without phenocrysts and bubbles for this photo); E – groundmass of porous area; F – groundmass of low-porosity area. A is a photomicrograph; B-F are BSE images – black areas are vesicles, dark grey plagioclase, mid-grey interstitial glass, light grey olivine and white is oxides.

Figure 6. Complex zoning patterns of microphenocrysts in lava of MGV. A - Oscillatory and sector zoning pattern of clinopyroxene in high-porosity areas; B - Oscillatory zoning of olivine microphenocryst in high-porosity area; C - Sector zoning of plagioclase phenocrysts in low-

porosity area; D - Clot of plagioclase, clinopyroxene and oxide crystals from low-porosity area close to boundary with porous area.

Figure 7. Groundmass BSE images from NGV lavas showing progressive textural evolution. Top row - volcanic bomb; middle row - hot-collected lava from active lava front (see Figure 1D); bottom row - naturally solidified lava.

Figure 8. Composition of olivine phenocrysts and microlites for different types of eruptive products of 2012-13 eruption in terms of MnO, NiO and CaO versus forsterite (Fo) content. Sample locations given in Table 1. "HP parts" corresponds to high-porosity areas containing the most Mg mineral paragenesis (see description in the text). Olivines from 1975-76 eruption (unpublished data Plechov) are shown for comparison

Figure 9. Composition of spinels from 2012-13 eruption. Spinels from 1975-76 eruption (unpublished data Plechov) are shown for comparison. "sp in ol" denotes spinel inclusions in olivine.

Figure 10. Summary of mineral composition for different rock varieties of 2012-13 eruption. HP and LP are high-porosity and low-porosity varieties of MGV lavas. NGV samples are tephras and lavas. Horizontal axis represent molar percent of forsterite and anorthite in olivine and plagioclase, respectively, and Mg# of clinopyroxene.

Figure 11. Selected major elements versus molar Mg# ($100*Mg/(Mg+Fe^{tot})$) for bulk rock, glass and reconstructed melt compositions of 2012-13 eruption. NGV samples: 1- reconstructed melts, 2 – whole rocks, 3- groundmass glasses from PK-13/4b (NGV bomb) 4 – groundmass glasses from PK-13/7 (NGV liquid lava front); MGV samples: 5 - whole rocks, 6 - groundmass glasses from high-porosity areas, 7 – groundmass glasses from low-porosity areas.

Fig 12. Volatile contents of olivine-hosted melt inclusions analysed by SIMS and electron microprobe. A. CO_2 versus H_2O in MI from naturally-quenched tephra, re-heated tephra, tephra groundmass and solidified, slow-cooled lava. Solid lines are isobars calculated after Newman and Lowenstern (2002). B Sulphur (as total S) versus H_2O. C Chlorine versus H_2O. D CO_2 versus K_2O (normalized to 100% volatile-free) for tephra melt inclusions showing extent of crystallization in response to decompression. Upper horizontal axis shows wt% crystallization relative to a parent melt with 2.44 wt% K_2O, assuming K is a perfectly incompatible element; right hand vertical axis shows calculated pressure at 1.1 wt% H_2O (from A). Note that two melt inclusions with less than 2 wt% K_2O are not shown on this plot. In B-D we also show MI

analyses from Kluchevskoy Group volcanoes for comparison using data sources given in Figure 13.

Figure 13. Comparative chemical variations of melt inclusions (MI) from 2013-13 eruption of Tolbachik and other Klyuchevskoy Group volcanoes. Data for 2012-13 tephra MI and groundmass (gmass lv) glass from this study (Table 7) and M&P,11 –Mironov & Portnyagin (2011); Auer,09 – Auer et al (2009); and P et al. - Portnyagin et al (2007) (a) CO_2 and H_2O. Dashed trends show illustrative open system degasing calculated using VolatileCalc 2.0 (Newman & Lowenstern, 2002). Note that displacement of Kluchevskoy MI from 2012-13 MI indicates different initial H2O contents that cannot be reconciles simply by degassing. (b) K_2O and H_2O. Note the two distinct two groups; high-K_2O and low-H_2O from the 2012-13 eruption and low-K_2O and high-H_2O (Kluchevskoy and 1975-76 Tolbachik eruption (Portnyagin et al. 2007). It is not possible to reconcile the differences between the two groups in terms of simple degassing or crystallization processes.

Tables

Table 1. Samples studied

Table 2. Bulk rock analyses of major elements

Table 3. Representative mineral analyses

Table 4. Interstitial (groundmass) glass analyses

Table 5. Modal proportions of different magma types.

Table 6. Fractionation calculations

Table 7. Glass compositions; melt inclusions and groundmass

Table 1. Samples studied

MSU No.	Bristol No.	Lat.	Long.	Cone	Lava field	Date*	Owner	Short description
Tolb2012	-	-	-	MGV	near cone	2012-Dec-26	V.M.Okrugin	Lava breccia collected near vent
PK-13/12	KAM 17	N 55°43’44.9’’	E 160°17’44.7’’	NGV	Leningradskoe	2013-Aug-18	P.Plechov	aa-lava
PK-13/7	KAM 12	N 55°43’29.3’’	E 160°21’09.7’’	NGV	Taludskoe	2013-Aug-17	P.Plechov	liquid lava on the lava front
-	KAM 20a	N 55°43’29.3’’	E 160°21’09.7’’	NGV	Taludskoe	2013-Aug-17	J.Blundy	liquid lava on the lava front
PK-13/6	KAM 10	N 55°43’44.0’’	E 160°19’56.4''	NGV	Taludskoe	2013-Aug-17	P.Plechov	toothpaste lava
PK-13/4	KAM 9	N 55°46’03.2’’	E 160°19’03.3’’	NGV	cone	2013-Aug-16	P.Plechov	Hot lava bomb
PK-13/4	KAM 8	N 55°46’03.2’’	E 160°19’03.3’’	NGV	cone	2013-Aug-16	P.Plechov	Hot lava bomb
PK-13/3	KAM 6	N 55°44’54.5’	E 160°18’54.4’’	NGV	Leningradskoe	2013-Aug-16	P.Plechov	Rope lavas
PK-13/2	KAM 5	N 55°44’40.9’’	E 160°18’55.6’’	NGV	Leningradskoe	2013-Aug-16	P.Plechov	toothpaste lava
PK-13/2	KAM 4	N 55°44’40.9’’	E 160°18’55.6’’	NGV	Leningradskoe	2013-Aug-16	P.Plechov	toothpaste lava
NK-13/2	-	N: 55^{o} 45.954’	E: 160^{o} 19.318’	NGV	near cone	2013-Aug-20	N.Nekrylov	Fresh ash
NK-13/3	-	N: 55^{o} 46.017’	E: 160^{o} 19.189’	NGV	cone	2013-Aug-20	N.Nekrylov	Fresh ash

* Date of collection

Table 2. Bulk rock analyses of major elements

Lab*	ETH	ETH	ETH	ETH	ETH	ETH	ETH	ETH	ETH	IGEM	IGEM	IGEM
Sample**	KAM 17	KAM 12	KAM 20a	KAM 10	KAM 9	KAM 8	KAM 6	KAM 5	KAM 4	PK-13-7	PK-13-4a	PK-13-6
SiO_2	51.82	51.67	51.86	51.92	51.76	51.90	52.18	52.06	51.79	51.28	51.27	50.97
TiO_2	1.96	1.95	1.95	1.97	1.95	1.96	1.97	1.96	1.96	1.94	1.95	1.94
Al_2O_3	16.11	16.12	16.10	16.15	16.07	16.13	16.17	16.16	16.13	16.61	16.38	17.08
FeO	10.58	10.56	10.52	10.55	10.46	10.47	10.64	10.53	10.54	10.47	10.63	10.41
MnO	0.20	0.20	0.19	0.19	0.18	0.18	0.20	0.19	0.19	0.17	0.17	0.17
MgO	4.22	4.27	4.30	4.24	4.28	4.27	4.25	4.26	4.21	4.01	4.08	3.73
CaO	7.46	7.46	7.44	7.44	7.44	7.46	7.47	7.47	7.46	7.47	7.49	7.43
Na_2O	3.63	3.62	3.61	3.64	3.60	3.66	3.65	3.65	3.65	3.45	3.40	3.67
K_2O	2.45	2.43	2.43	2.46	2.44	2.44	2.47	2.47	2.45	2.40	2.44	2.41
P_2O_5	0.73	0.72	0.73	0.73	0.73	0.73	0.74	0.73	0.73	0.69	0.68	0.71
Total	99.16	99.00	99.14	99.29	98.90	99.18	99.74	99.47	99.12	98.49	98.49	98.52
Mg#	41.7	42.0	42.3	41.8	42.3	42.2	41.7	42.0	41.7	40.7	40.7	39.1
Alk	6.07	6.05	6.05	6.09	6.04	6.09	6.12	6.12	6.11	5.85	5.84	6.08

* Laboratory where analysis was poduced: ETH - ETH Zhurich, IGEM - IGAM RAS Moscow.

** Original sample name, see Tabl.1 for description.

Table 3. Representative mineral analyses

Averaged analyses of Olivine

Analysis No.	1	2	3	4	5	6	7
Sample No.	Tolb2012	Tolb2012	Tolb2012	Tolb2012	NK-13-2, 13-3	PK-13-6	PK-13-7
N	4	1	1	3	29	6	12
Mg#, mol.%	86.70	73.03	76.62	67.70	73.22	72.92	73.64
Fo, mol.%	85.75	72.10	75.80	66.80	72.55	72.22	72.93
SiO_2	39.31	37.36	37.62	36.30	37.62	37.73	37.69
TiO_2	0.02	0.02	0.02	0.05	0.02	0.02	0.02
Al_2O_3	-	-	-	-	0.03	0.02	0.03
FeO	12.55	23.97	21.22	28.25	24.46	24.61	23.49
MnO	0.23	0.40	0.32	0.53	0.38	0.40	0.38
MgO	45.89	36.41	39.02	33.21	37.54	37.20	36.84
CaO	0.24	0.31	0.19	0.29	0.23	0.23	0.24
NiO	0.22	0.10	0.19	0.04	0.12	0.13	0.12
Cr_2O_3	0.09	0.00	0.10	0.04	-	-	-
P_2O_5	0.03	0.07	0.23	0.26	0.04	0.05	0.03
Total	98.70	98.80	99.00	99.07	100.44	100.41	98.84

Analysis No	8	9	10	11	12	13
Sample No.	NK-13-2	NK-13-2	PK-13/4b	PK-13/7	PK-13/7	PK-13/7
N	11	9	8	1	1	7
Mg#, mol.%	73.48	73.54	68.75	75.22	72.05	68.79
Fo, mol.%	72.78	72.85	67.75	74.37	71.26	67.80
SiO_2	37.19	37.44	36.83	38.22	37.72	36.80
TiO_2	-	-	0.06	0.02	0.04	0.05
Al_2O_3	-	-	-	-	-	-
FeO	23.46	23.58	26.65	21.83	24.35	26.67
MnO	0.37	0.37	0.52	0.37	0.45	0.50
MgO	36.47	36.78	32.89	37.17	35.22	32.99
CaO	0.22	0.22	0.32	0.23	0.24	0.32
NiO	0.11	0.10	0.07	0.10	0.01	0.06

Cr_2O_3	-	-	-	-	-	-
P_2O_5	-	-	0.22	0.09	0.10	0.20
Total	97.90	98.56	97.70	98.18	98.25	97.75

1-2 Ol in high-porosity areas (1-cores, 2 - rims); 3-4 Ol in low-porosity areas (3 -cores, 4 - rims); 5-9 - Ol hosted MI (5-7), CPx (8) and Pl(9); 10 - Ol microphenocrysts; 11-13 - Ol in quenched lava (11-cores, 12 - rims, 13 - microphenocrysts)

Averaged analyses of Plagioclase

Analysis No	1	2	3	4	5	6	7
Sample	NK-13-2	Tolb2012	Tolb2012	Tolb2012	Tolb2012	Tolb2012	PK-13/4b
N	13	3	3	3	3	1	1
An., mol.%	78.23	54.14	59.10	70.27	77.04	57.32	63.79
SiO_2	46.98	53.97	52.89	50.06	48.31	53.22	51.79
Al_2O_3	32.14	27.63	28.85	30.30	32.15	28.35	30.33
FeO	1.24	1.02	0.94	1.25	0.72	0.93	0.73
MgO	0.09	-	-	-	-	-	0.17
CaO	15.64	11.07	12.29	14.43	15.70	11.83	13.15
Na_2O	2.26	4.75	4.42	3.20	2.47	4.58	3.78
K_2O	0.14	0.60	0.40	0.23	0.15	0.40	0.30
BaO	-	0.16	0.13	0.09	0.09	0.14	0.08
Total	98.47	99.20	99.92	99.57	99.59	99.45	100.34

Analysis No	8	9	10	11	12	13
Sample	PK-13/4b	PK-13/7	PK-13/7	PK-13/6	PK-13/6	PK-13/6
N	7	2	7	2	1	2
An., mol.%	56.51	63.60	55.79	77.80	66.67	56.64
SiO_2	53.85	52.27	54.12	47.61	50.05	52.67
Al_2O_3	28.79	30.33	28.84	31.71	29.67	27.85
FeO	1.10	0.87	1.05	0.80	0.88	0.95

MgO	0.17	0.19	0.18	-	-	-
CaO	11.58	13.22	11.51	15.73	13.32	11.49
Na_2O	4.39	3.80	4.47	2.36	3.47	4.48
K_2O	0.57	0.33	0.59	0.19	0.32	0.55
BaO	0.14	0.10	0.18	-	-	0.21
Total	100.59	101.07	100.95	98.38	97.71	98.09

1 - Pl inclusions in olivine; 2-4 - Pl microlites in low porosity(2), porous(3) and high-porosity(4) areas;
5-6 - Pl phenocrysts in low-porosity areas (5 - cores, 6 - rims); 7 & 9 - Cores of Pl microphenocrysts;
8 & 10 - Pl microlites; 11-13 - Pl from toothpaste lava (11 - cores, 12 - rims, 13 - microlites)

Averaged analyses of Clinopyroxenes

Analysis No Sample	1 NK-13-2	2 Tolb2012	3 Tolb2012	4 Tolb2012	5 PK-13/6
N	7	3	1	2	10
Mg #	80.28	89.64	82.94	81.72	76.42
SiO_2	50.01	51.32	51.44	49.86	49.09
TiO_2	1.00	0.58	0.60	1.21	1.41
Al_2O_3	3.47	3.05	2.53	3.37	3.29
FeO	9.02	6.10	8.44	8.81	10.69
MnO	0.22	0.20	0.26	0.22	0.27
MgO	14.90	16.64	16.49	14.35	14.23
CaO	20.15	21.48	19.55	21.25	19.15
Na_2O	0.34	0.23	0.28	0.42	0.43
Cr_2O_3		0.22	0.00		
Total	99.15	99.82	99.59	99.50	98.55

1 - Cpx inclusions in olivine; 2-3 - CPx in high-porosity areas (2 - Cores, 3 - rims);
4 - Cpx cores in low-porosity areas; 5 - CPx microlites in NGV lava

Averaged analyses of oxide minerals

Analysis No Sample	1 Tolb2012	2 Tolb2012	3 PK-13/4b	4 PK-13/4b	5 PK-13/7	6 PK-13/7	7 PK-13/6	8 PK-13/6
N	2	2	3	5	4	4	3	4
Cr #	58.00	2.89	10.35	0.76	7.73	0.94	8.95	0.81
SiO_2	0.41	0.20	0.17	0.22	0.21	0.20	0.19	0.21
TiO_2	0.92	12.61	9.72	12.87	12.04	12.94	12.31	13.59
Al_2O_3	12.21	4.45	7.27	4.44	4.34	4.22	4.27	3.81
Cr_2O_3	42.07	1.31	5.33	0.34	3.60	0.42	4.02	0.34
FeO	29.99	72.38	66.24	70.91	69.56	71.50	68.14	70.87
MnO	0.45	0.38	0.36	0.36	0.39	0.39	0.42	0.39
MgO	9.88	3.51	4.99	4.58	4.57	4.55	4.36	4.04
CaO	0.07	0.05	0.11	0.17	0.10	0.14	0.10	0.12
NiO	0.11	0.02	0.15	-	-	-	-	-
ZnO	0.30	0.31	-	-	-	-	-	-
Total	96.40	95.23	94.16	93.85	94.67	94.33	93.74	93.34

1 - Cr-Sp inclusions in olivine of high-porosity areas; 2 - Ti-Mt from low-porosity areas; 3, 5 & 7 - Cores of Ti-Mt microphenocrysts;
4, 6 & 8 - Rims of Ti-Mt microphenocrysts.

Table 4. Interstitial (groundmass) glass analyses

Sample	Tolb2012		Tolb2012		Tolb2012		PK-13/4b		PK-13/7	
Description	LP		P		HP		HLB		LL	
N	3	s.d	3	s.d	3	s.d	20	s.d	20	s.d
SiO_2	58.21	*0.4*	54.31	*0.2*	54.26	*0.1*	52.22	*0.3*	53.19	*0.3*
TiO_2	2.02	*0.04*	1.92	*0.05*	1.76	*0.05*	2.29	*0.05*	2.39	*0.04*
Al_2O_3	14.53	*0.2*	16.18	*0.2*	17.03	*0.4*	14.83	*0.2*	14.44	*0.2*
FeO	8.66	*0.3*	9.10	*0.3*	8.77	*0.1*	10.75	*0.1*	10.83	*0.1*
MnO	0.18	*0.03*	0.17	*0.02*	0.17	*0.05*	0.20	*0.03*	0.23	*0.04*
MgO	1.69	*0.11*	3.13	*0.07*	2.94	*0.16*	3.41	*0.06*	3.30	*0.07*
CaO	3.75	*0.1*	6.61	*0.1*	7.27	*0.2*	6.95	*0.1*	6.91	*0.1*
Na_2O	4.20	*0.31*	4.34	*0.12*	4.25	*0.07*	3.45	*0.08*	3.52	*0.08*
K_2O	5.06	*0.12*	3.13	*0.15*	2.71	*0.03*	2.77	*0.03*	3.00	*0.07*
P_2O_5	1.31	*0.03*	0.83	*0.04*	0.68	*0.02*	1.05	*0.06*	1.14	*0.06*
Cl	0.10	*0.02*	0.05	*0.01*	0.04	*0.01*	0.04	*0.02*	0.04	*0.01*
Total	99.70	*0.6*	99.77	*0.6*	99.88	*0.2*	97.96	*0.5*	98.98	*0.5*
Mg #	0.26		0.38		0.37		0.36		0.35	
Na_2O+K_2O	9.26		7.47		6.96		6.22		6.52	
Na_2O-2	2.20		2.34		2.25		1.45		1.52	

* LP - Low porosity; P - porous; HP - high porosity; HLB - hot lava bomb; LL - liquid lava

Table 5. Modal proportions of different magma types

Sample	PK-13/4b		PK-13/7		PK-13/6***
N	12	sd	11	sd	~500 counts
Pl	10.4	*2.2*	20.8	*2.2*	30.7
Gl	34.8	*8.6*	69.8	*5.6*	52.4

Ore	0.3	*0.1*	0.7	*0.2*	1.8
Ol	1.0	*0.4*	2.7	*0.9*	6.8
Porosity	53.5	*10.9*	6.0	*6.7*	8.2
Pl*	22.7	*2.3*	22.2	*2.3*	33.5
Gl*	74.5	*2.1*	74.2	*1.9*	57.1
Ore*	0.5	*0.2*	0.8	*0.3*	1.9
Ol*	2.2	*0.7*	2.8	*0.8*	7.5
Crystallinity	25.5	*2.1*	25.8	*1.9*	42.9
Pl/Ol proportion	10.2		7.8		4.5
Viscosity, poise**	28249		9268		20039

* values without pores

** effective viscocity calculated after [Marsh, 1981] with melt viscosity calculated by [Bottinga & Weill, 1972] at 1100 ^{o}C

*** calculated by point counting method in thin section. Tiny cristallized groundmass was calculated as glass.

Table 6. Fractionation calculations

Sample Type of material	PK-13/4b Glass	PK-13/7 Glass	PK-13/7 Ol	PK-13/7 Pl	PK-13/7 Mt	Calculated composition -
SiO_2	53.33	53.76	37.66	53.70	0.21	53.79
TiO_2	2.34	2.42	0.06	0.00	13.77	2.42
Al_2O_3	15.15	14.59	0.16	28.62	4.50	14.61
FeO	10.97	10.95	27.30	1.04	76.11	10.97
MnO	0.21	0.23	0.51	0.00	0.42	0.21
MgO	3.49	3.34	33.77	0.18	4.84	3.34
CaO	7.10	6.98	0.33	11.42	0.15	6.97
Na_2O	3.52	3.55	0.00	4.44	0.00	3.53
K_2O	2.83	3.03	0.00	0.59	-	3.00
P_2O_5	1.07	1.15	0.21	0.00	-	1.15
Total	100.00	100.00	100.00	100.00	100.00	100.00
Crystallization, wt. %	-	-	1	5.3	0.6	-

Crystallization, vol. %	-	-	0.7	5.4	0.3	-

*All data are normalized to 100%

Table 7. Glass compositions; melt inclusions and groundmass

Sample	NK-13-2																
Inclusion	2-5-2-b	2-4-7	2-4-6	2-3-4	2-3-3	2-2-12a	2-2-12b	3-5-4a	3-5-4b	3-5-3	3-4-1	2-9-8b	2-8-7	2-6-12	3-9-7	2-5-3	2-8-7*	2-6-12*
Length, μm	160	43	56	72	112	91	148	144	103	91	38	41	67	78	66	70	-	-
Width, μm	95	27	51	50	102	51	58	54	67	46	25	31	55	69	60	48	-	-
Bubble diameter, μm	-	-	-	-	-	-	-	-	-	-	-	-	-	-	-	16	-	-
SiO_2	50.10	52.27	51.06	50.71	50.98	51.48	51.09	50.73	50.64	50.83	51.02	46.36	50.24	51.45	52.18	50.83	50.65	n.d
TiO_2	1.98	2.03	1.90	1.81	1.95	1.88	2.04	2.01	1.82	1.92	1.85	1.71	2.03	1.94	1.91	1.64	2.96	n.d
Al_2O_3	15.75	16.94	15.85	16.04	15.50	15.84	15.70	15.60	16.16	15.74	16.04	14.59	15.25	16.10	15.89	15.19	14.30	n.d
FeO	11.01	10.37	10.92	10.42	10.62	10.39	10.47	10.67	10.52	10.40	10.93	11.01	10.92	10.34	10.64	11.10	11.06	n.d
MnO	0.19	0.19	0.14	0.16	0.19	0.19	0.20	0.16	0.17	0.18	0.16	0.19	0.12	0.18	0.19	0.20	0.20	n.d
MgO	3.84	3.38	3.96	4.21	4.03	3.78	3.88	3.94	3.59	4.09	3.92	4.44	4.08	3.83	3.95	4.16	3.92	n.d
CaO	7.33	7.55	7.16	7.83	7.19	7.34	7.21	7.27	7.36	7.25	7.43	7.32	7.28	7.31	7.29	7.12	6.95	n.d
Na_2O	3.78	3.48	3.59	3.62	3.52	3.56	3.62	3.61	3.90	3.48	3.26	4.34	3.64	3.48	3.46	3.72	3.71	n.d
K_2O	2.61	2.49	2.38	2.31	2.42	2.39	2.37	2.40	2.73	2.33	2.29	2.46	2.32	2.46	2.33	2.43	2.75	n.d
P_2O_5	0.63	0.80	0.70	0.66	0.66	0.71	0.74	0.84	0.82	0.75	0.72	0.86	0.73	0.82	0.75	1.20	0.93	n.d
Cr_2O_3	0.02	0.01	0.00	0.01	0.01	0.01	0.01	0.01	0.01	0.00	0.00	0.01	0.01	0.01	0.01	0.01	0.00	n.d
NiO	0.03	0.03	0.03	0.02	0.01	0.01	0.01	0.03	0.01	0.01	0.00	0.02	0.06	0.00	0.02	0.01	0.00	n.d

S	0.013	0.034	0.035	0.039	0.025	0.047	0.028	0.030	0.015	0.037			0.025	0.027	0.033	0.063	0.010	n.d
Cl	0.050	0.068	0.048	0.043	0.053	0.047	0.052	0.046	0.053	0.055	0.056	0.068	0.051	0.047	0.064	0.069	0.050	n.d
Total	97.32	99.61	97.75	97.84	97.11	97.63	97.39	97.33	97.80	97.04	97.69	93.37	96.72	97.97	98.68	97.67	96.81	n.d
Ol-Host Mg#	74.26	72.60	73.01	74.79	73.16	72.85	72.70	73.23	73.57	73.92	73.03	73.00	73.22	73.49	72.66	72.71	n.d	n.d
H_2O Raman	1.09	0.48	0.97	1.14	1.11	1.11	1.17	1.05	n.d	1.06	1.07	0.68	1.08	1.12	1.00	1.09	n.d	n.d
H_2O, wt%, SIMS	0.45	n.d	1.10	1.31	1.26	1.15	1.24	1.19	n.d	1.35	n.d	n.d	1.03	1.13	1.32	1.31	0.31	n.d
sd	0.02	n.d	0.03	0.04	0.04	0.06	0.03	0.12	n.d	0.03	n.d	n.d	0.03	0.09	0.05	0.03	0.01	n.d
CO_2, ppm, SIMS	88	n.d	331	411	396	428	398	723	195	262	n.d	n.d	414	204	408	154	62	46
sd	19	n.d	31	27	23	25	29	30	24	24	n.d	n.d	25	21	29	24	21	17
P, bars**	212	-	833	1056	1010	1048	1009	1653	-	753	-	-	990	570	1052	508	145	-
Sample	NK-13-2-HF-H						NK-13-3											
Inclusion	2-5a	2-5b	10-13b	3-1a	5-15a	2-1a	2-1b	b	1-8-12	1-5-6	1-5-4	1-5-1	1-2-8	1-13-4	1-9-10	1-6-12b	1-6-6a	1-6-6b
Length, μm	106	75	56	59	114	75	75	48	91	69	53	83	82	57	64	139	65	64
Width, μm	70	45	43	41	73	51	51	31	76	46	51	37	55	45	48	92	34	59
Bubble diameter, μm	-	-	-	-	21	18	18	11	-	-	-	17	-	-	-	-	10	-

SiO_2	49.38	48.38	50.06	n.d	n.d	n.d	n.d	n.d	51.57	51.33	51.01	49.73	51.14	51.30	50.16	51.08	51.50	51.47
TiO_2	1.94	2.12	1.90	n.d	n.d	n.d	n.d	n.d	1.83	1.87	1.96	1.86	1.89	1.99	1.86	1.96	1.76	1.91
Al_2O_3	13.60	13.63	14.77	n.d	n.d	n.d	n.d	n.d	15.83	15.78	15.82	16.31	15.92	16.12	15.47	16.35	15.93	15.87
FeO	12.76	13.70	11.19	n.d	n.d	n.d	n.d	n.d	10.53	10.35	10.60	9.35	11.02	10.50	10.50	10.42	10.61	10.51
MnO	0.22	0.27	0.23	n.d	n.d	n.d	n.d	n.d	0.20	0.16	0.26	0.19	0.17	0.17	0.15	0.16	0.19	0.17
MgO	5.79	5.63	4.93	n.d	n.d	n.d	n.d	n.d	4.03	3.93	4.13	4.05	3.88	3.91	4.16	3.56	3.77	3.84
CaO	6.01	6.42	7.58	n.d	n.d	n.d	n.d	n.d	7.32	7.35	7.35	8.25	7.42	7.29	7.33	7.59	7.36	7.19
Na_2O	3.40	3.32	3.34	n.d	n.d	n.d	n.d	n.d	3.59	3.55	3.46	3.67	3.35	3.46	3.72	3.58	3.74	3.74
K_2O	2.50	2.31	2.09	n.d	n.d	n.d	n.d	n.d	2.41	2.44	2.34	2.18	2.30	2.39	2.34	2.59	2.34	2.41
P_2O_5	0.84	0.85	0.71	n.d	n.d	n.d	n.d	n.d	0.70	0.65	0.72	0.64	0.75	0.81	0.77	0.82	0.78	0.79
Cr_2O_3	0.01	0.01	0.01	n.d	n.d	n.d	n.d	n.d	0.01	0.01	0.02	0.01	0.01	0.00	0.01	0.00	0.01	0.01
NiO	0.01	0.02	0.03	n.d	n.d	n.d	n.d	n.d	0.01	0.03	0.00	0.02	0.02	0.03	0.05	0.02	0.02	0.00
S	0.015	0.028	0.045	n.d	n.d	n.d	n.d	n.d	0.026	0.037	0.031	0.059	0.026	0.024	0.023	0.032	0.038	0.042
Cl	0.045	0.055	0.032	n.d	n.d	n.d	n.d	n.d	0.022	0.059	0.046	0.059	0.056	0.040	0.059	0.047	0.052	0.044
Total	96.50	96.71	96.87	n.d	n.d	n.d	n.d	n.d	98.06	97.51	97.72	96.31	97.94	98.02	96.57	98.18	98.05	97.97
Ol-Host Mg#	71.84	71.81	73.57	n.d	n.d	n.d	n.d	n.d	72.57	73.75	73.74	75.89	72.93	72.61	73.55	72.87	72.76	73.27
H_2O Raman	1.19	1.12	1.64	1.41	1.05	1.09	1.09	0.95	1.23	1.15	1.24	1.17	0.78	1.09	1.27	0.91	1.45	n.d
H_2O, wt%, SIMS	n.d	n.d	n.d	1.01	1.14	1.19	1.00	0.95	1.28	1.15	1.45	n.d	0.90	1.35	1.34	0.54	n.d	1.33
sd	n.d	n.d	n.d	0.03	0.03	0.06	0.07	0.02	0.03	0.04	0.04	n.d	0.02	0.02	0.05	0.01	n.d	0.06
CO_2, ppm, SIMS	721	883	426	179	445	139	96	331	308	365	249	223	351	438	376	256	n.d	286
sd	55	52	48	19	34	23	29	34	30	26	23	24	26	31	28	40	n.d	31

P, bars**	1649	1944	1195	592	1080	444	306	800	831	916	755	620	832	1123	991	581	-	798
Sample			PK-13-6						PK-13-7									
Inclusion	1-4-9*	1-4-9a*	6-17a	13-7	13-6	12-14	13-3	8-22	1-1	1-2	1-4	1-5	1-6	1-7	1-8	1-9	2-1	2-2
Length, μm	-	-	63	118	49	65	93	85	53	41	74	95	50	62	47	36	50	42
Width, μm	-	-	46	49	33	53	88	67	42	34	50	58	47	61	32	34	41	36
Bubble diameter, μm	-	-	10	-	9	12	20	14	-	7	-	18	10	12	8	8	11	10
SiO_2	51.35	51.35	52.07	51.19	51.51	52.76	51.61	52.89	51.31	52.60	54.08	52.61	53.49	51.81	52.22	51.20	51.37	51.78
TiO_2	2.20	2.20	2.34	2.16	2.06	1.98	1.88	1.97	2.02	1.93	2.24	1.73	1.88	1.93	2.18	2.12	1.99	2.08
Al_2O_3	14.73	14.73	16.93	17.21	17.62	17.45	16.92	17.66	16.81	16.83	15.54	16.94	15.87	16.97	17.02	16.94	17.14	17.26
FeO	10.85	10.85	9.95	8.98	9.01	9.69	9.83	9.53	10.60	10.44	10.40	10.30	10.96	10.49	10.34	10.72	10.46	10.23
MnO	0.18	0.18	0.11	0.16	0.14	0.15	0.16	0.15	0.18	0.17	0.16	0.17	0.19	0.18	0.16	0.19	0.16	0.19
MgO	3.84	3.84	2.59	2.17	2.03	2.60	2.53	2.13	4.30	4.31	3.88	3.94	3.78	4.15	4.06	4.34	4.35	3.91
CaO	7.07	7.07	8.01	8.70	8.64	8.29	8.36	8.42	7.65	7.50	6.28	7.27	6.26	7.65	7.53	7.65	7.87	7.60
Na_2O	3.84	3.84	3.92	4.24	4.04	3.78	3.89	3.97	3.61	3.15	3.75	3.76	3.78	3.73	3.04	3.81	3.64	3.74
K_2O	2.70	2.70	2.59	2.90	2.44	2.51	2.42	2.58	2.62	2.28	2.69	2.46	2.86	2.31	2.47	2.24	2.18	2.35
P_2O_5	0.88	0.88	0.92	0.81	0.78	0.80	0.83	0.84	0.84	0.74	0.92	0.74	0.86	0.72	0.91	0.71	0.77	0.80
Cr_2O_3	0.01	0.01	0.00	0.01	0.02	0.01	0.02	0.01	n.d	n.d	n.d	n.d	n.d	n.d	n.d	n.d	n.d	n.d
NiO	0.00	0.00	0.01	0.02	0.00	0.03	0.02	0.01	n.d	n.d	n.d	n.d	n.d	n.d	n.d	n.d	n.d	n.d
S	n.d	n.d	0.032	0.014	0.056	0.027	0.048	0.040	n.d	n.d	n.d	n.d	n.d	n.d	n.d	n.d	n.d	n.d
Cl	0.037	0.037	0.037	0.049	0.074	0.058	0.068	0.081	0.041	0.056	0.047	0.071	0.048	0.057	0.059	0.087	0.048	0.048

Total	97.70	97.70	99.48	98.59	98.37	100.10	98.53	100.24	100	100	100	100	100	100	100	100	100	100
Ol-Host Mg#	n.d	n.d	73.03	73.61	73.33	72.60	73.20	71.73	74.26	74.18	73.72	73.53	70.28	74.58	74.37	73.98	74.30	74.71
H_2O Raman	n.d	n.d	0.21	0.24	0.19	0.17	0.11	0.18	n.d	n.d	n.d	n.d	n.d	n.d	n.d	n.d	n.d	n.d
H_2O, wt%, SIMS	0.26	0.32	0.12	0.11	0.19	n.d	0.13	0.12	n.d	n.d	n.d	n.d	n.d	n.d	n.d	n.d	n.d	n.d
sd	0.02	0.02	0.00	0.00	n,d	n.d	0.00	0.01	n.d	n.d	n.d	n.d	n.d	n.d	n.d	n.d	n.d	n.d
CO_2, ppm, SIMS	69	53	732	284	133	166	130	109	n.d	n.d	n.d	n.d	n.d	n.d	n.d	n.d	n.d	n.d
sd	21	22	32	29	26	27	28	26	n.d	n.d	n.d	n.d	n.d	n.d	n.d	n.d	n.d	n.d
P, bars**	158	126	1529	614	293	364	285	239	-	-	-	-	-	-	-	-	-	-

Sample Inclusion	2-4	2-5	2-6	2-8
Length, μm	80	53	42	62
Width, μm	48	50	34	38
Bubble diameter, μm	-	13	-	14
SiO_2	53.33	51.46	50.40	51.51
TiO_2	2.12	2.08	2.49	2.04
Al_2O_3	15.49	17.02	15.78	17.21
FeO	11.04	10.65	12.63	10.42
MnO	0.20	0.18	0.25	0.18
MgO	3.87	4.22	4.44	4.27
CaO	6.76	7.68	7.50	7.42
Na_2O	3.69	3.47	3.26	3.81

K_2O	2.58	2.36	2.03	2.34
P_2O_5	0.87	0.83	1.15	0.75
Cr_2O_3	n.d	n.d	n.d	n.d
NiO	n.d	n.d	n.d	n.d
S	n.d	n.d	n.d	n.d
Cl	0.046	0.060	0.059	0.053
Total	100	100	100	100
Ol-Host Mg#	72.54	75.16	72.44	74.15
H_2O Raman	n.d	n.d	n.d	n.d
H_2O, wt%, SIMS	n.d	n.d	n.d	n.d
sd	n.d	n.d	n.d	n.d
CO_2, ppm, SIMS	n.d	n.d	n.d	n.d
sd	n.d	n.d	n.d	n.d
P, bars**	-	-	-	-

* - groundmass glass, tephra; ** - Newman & Lowenstern, 2002; n.d - not determined

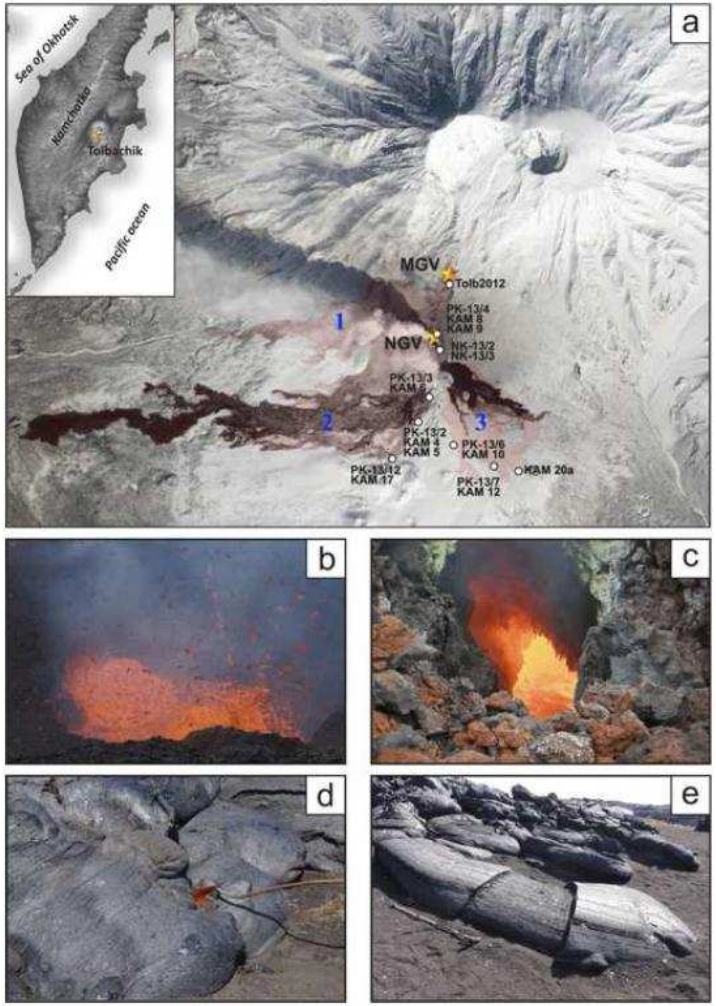

Figure 1

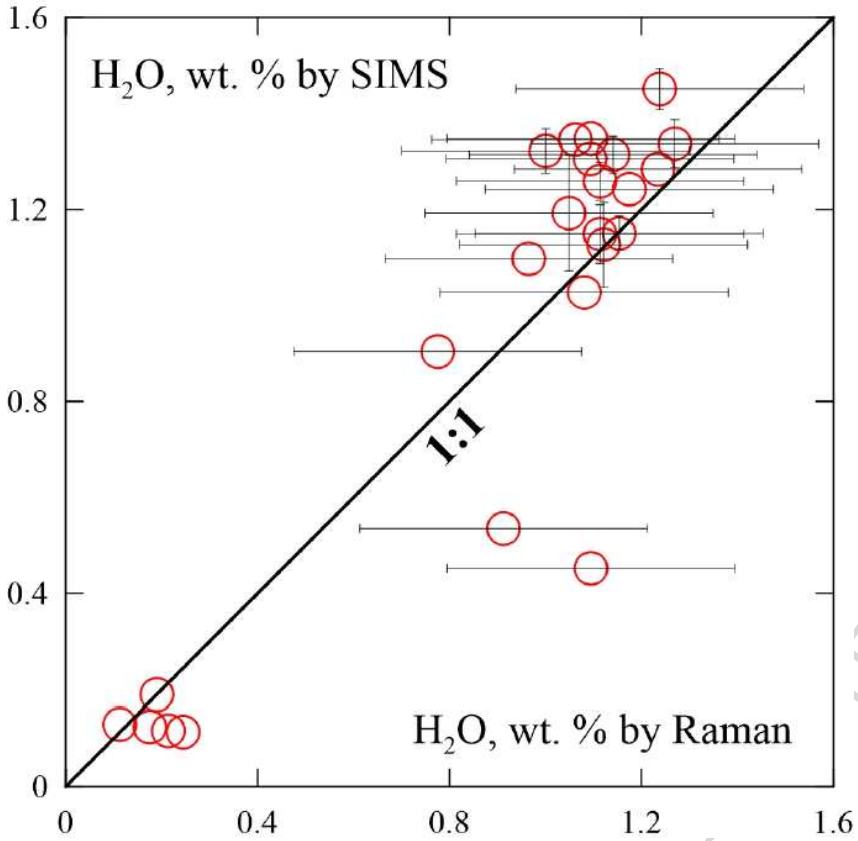

Figure 2

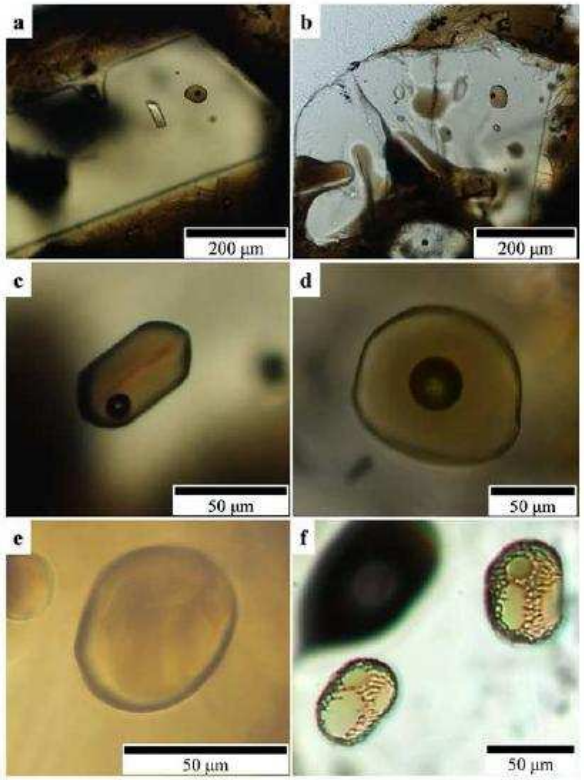

Figure 3

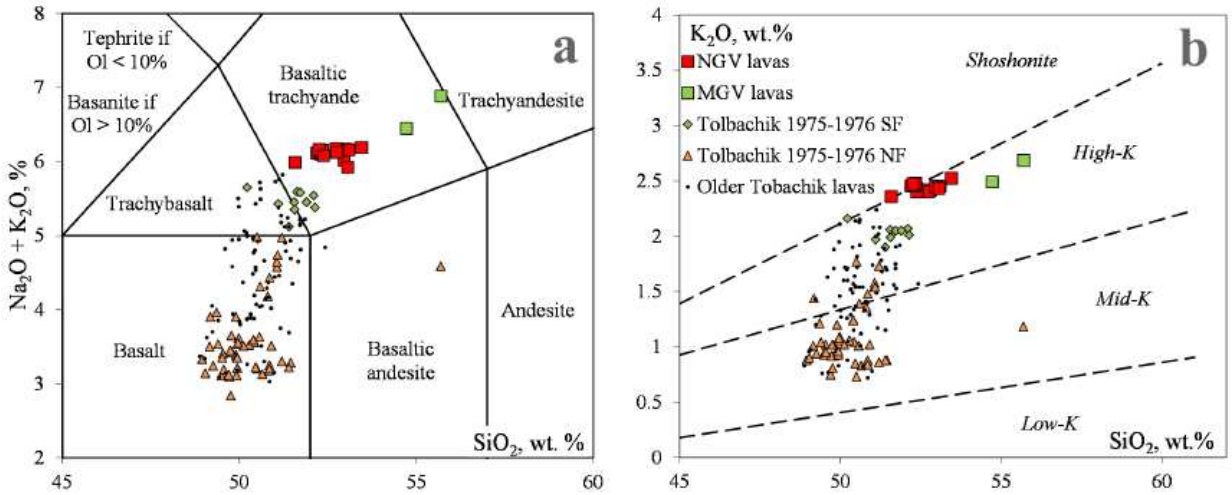

Figure 4

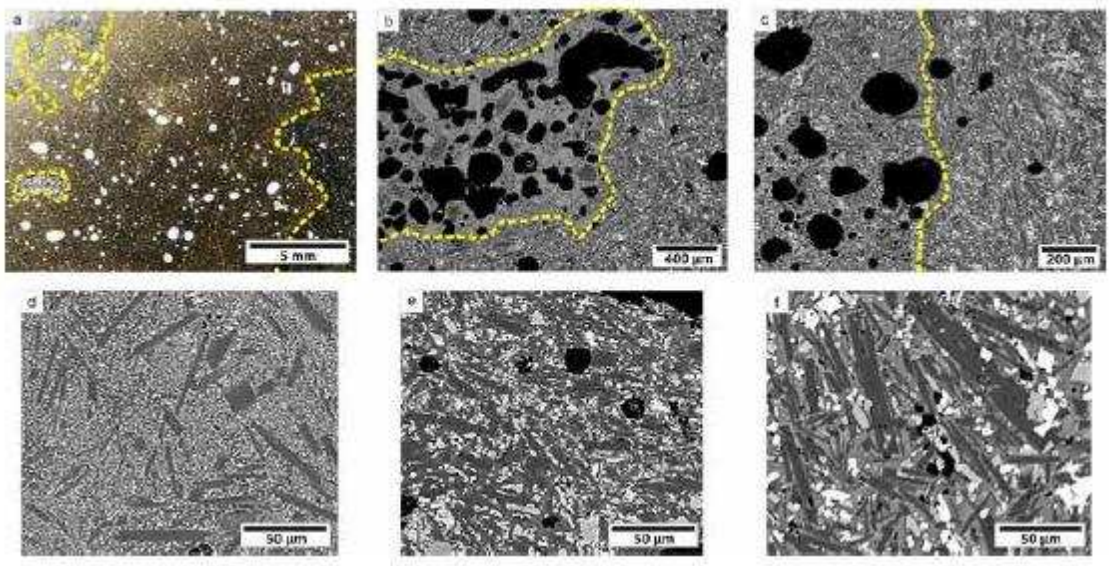

Figure 5

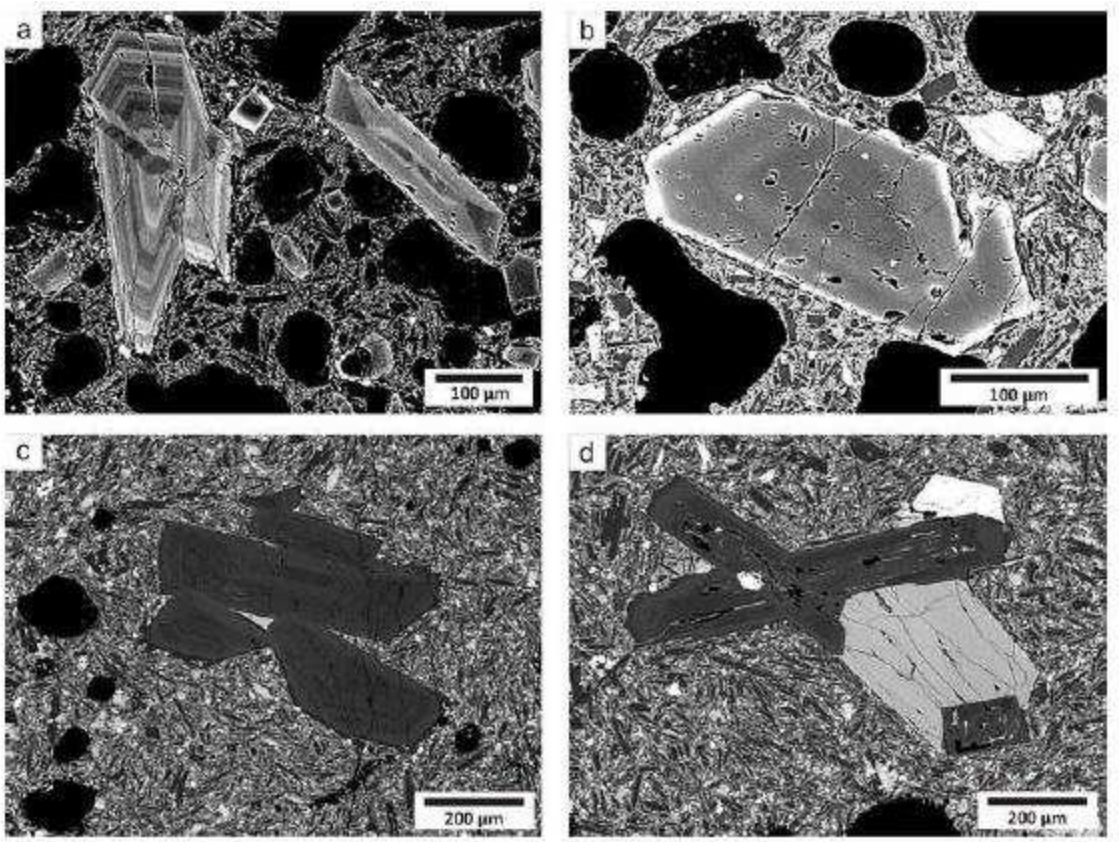

Figure 6

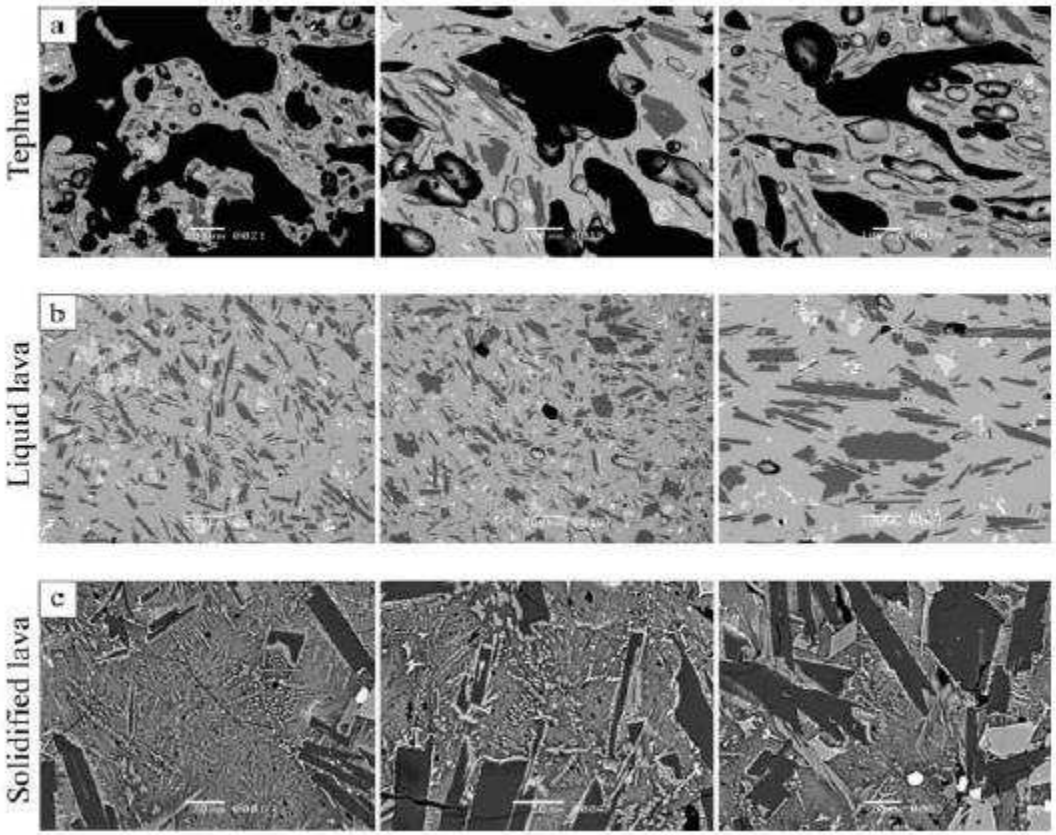

Figure 7

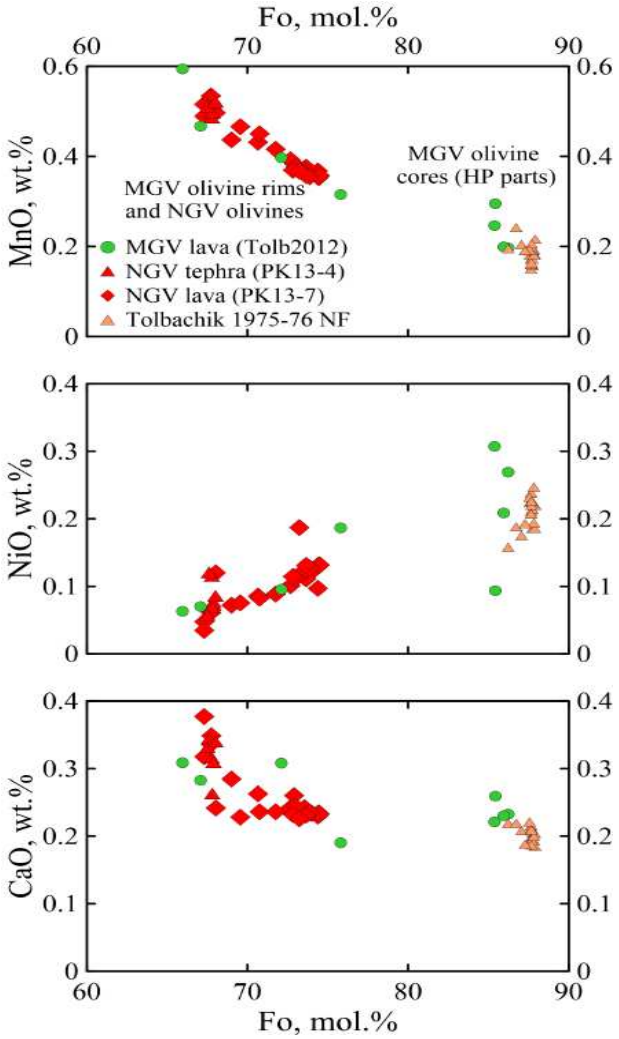

Figure 8

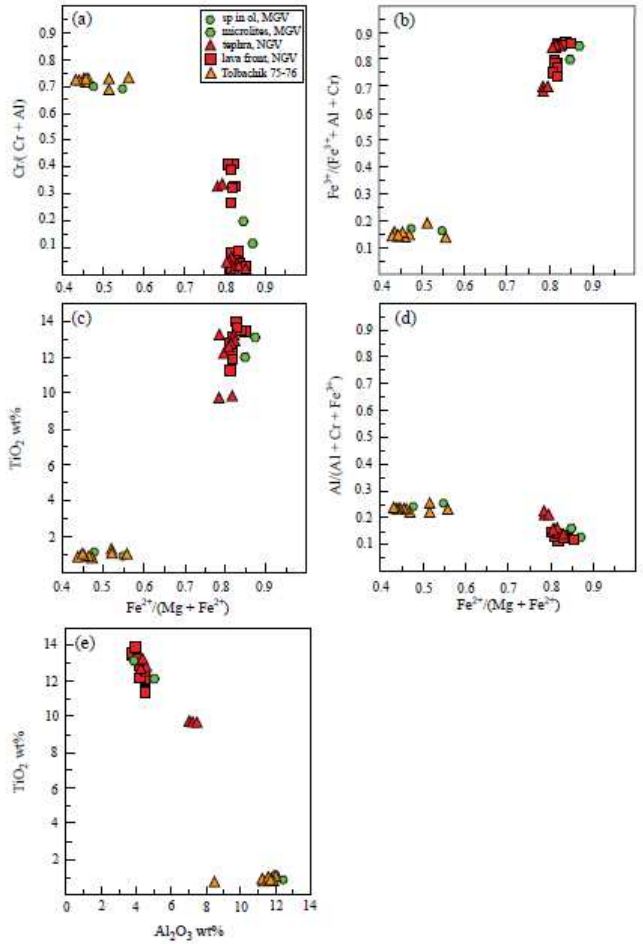

Figure 9

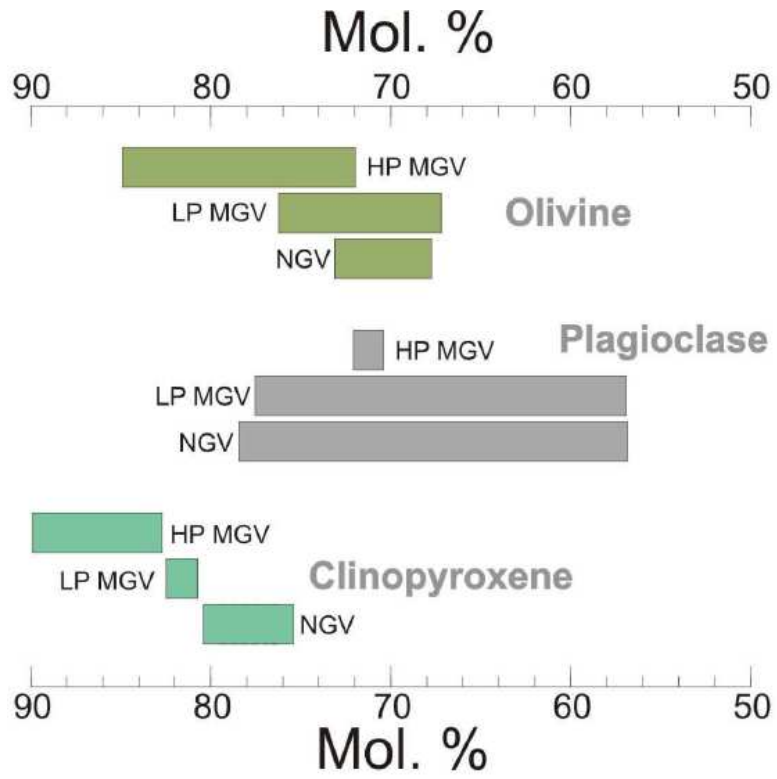

Figure 10

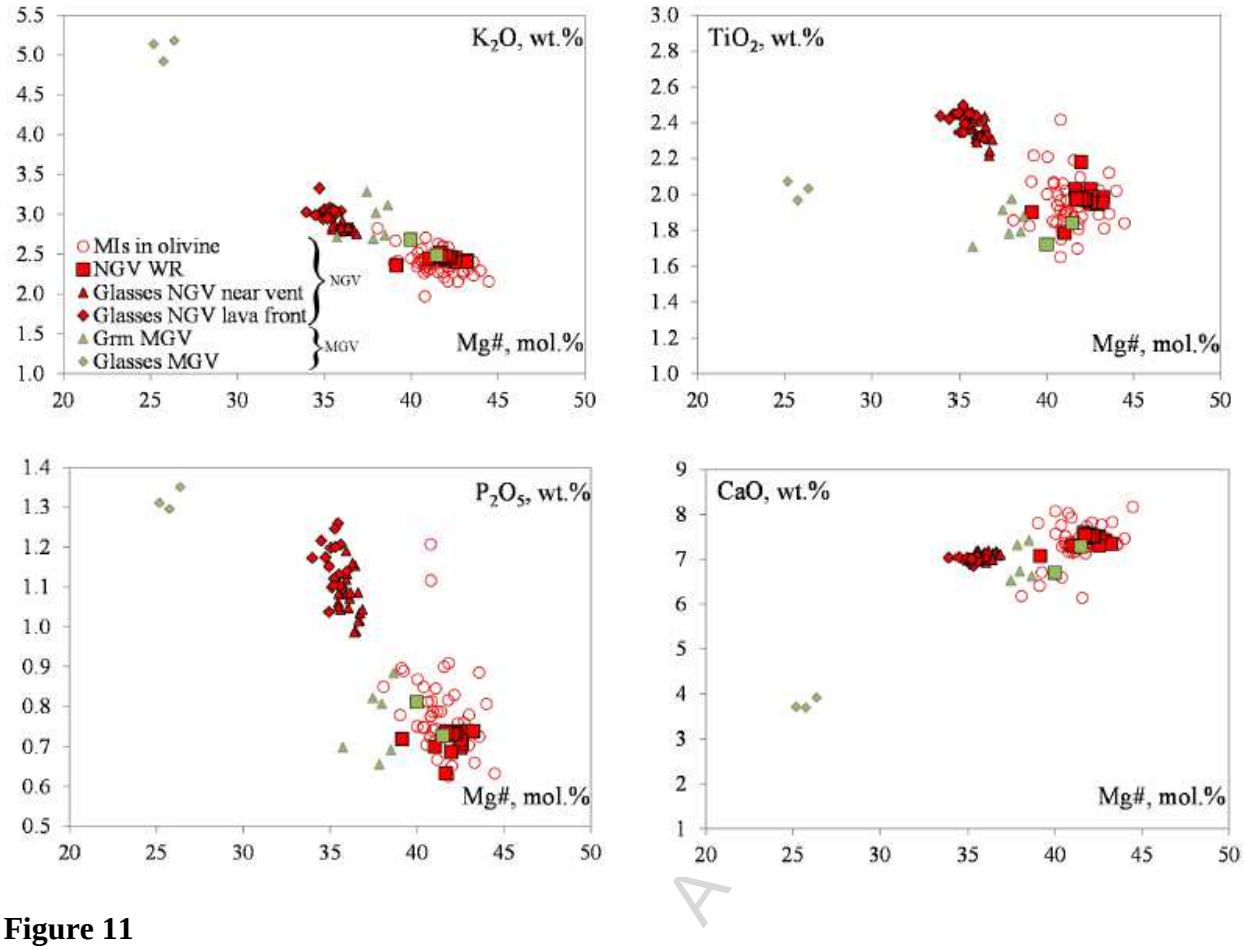

Figure 11

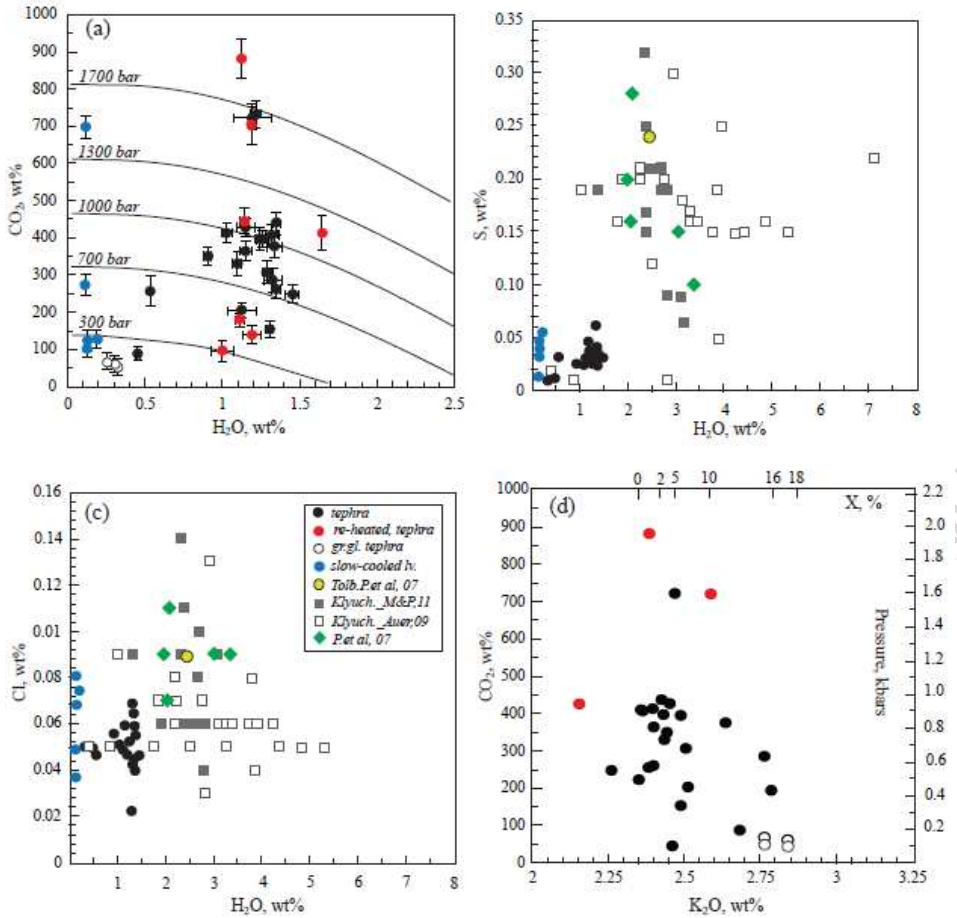

Figure 12

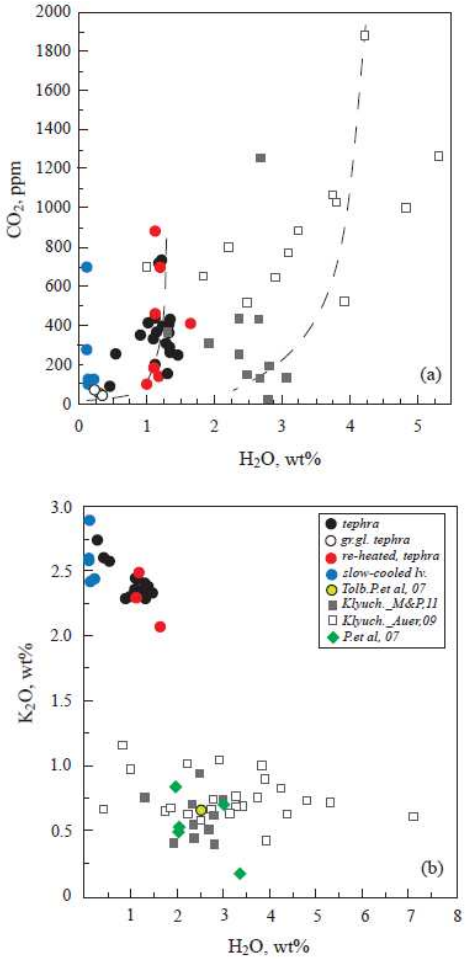

Figure 13